

# A discontinuous Galerkin solver for Boltzmann Poisson systems in nano devices<sup>1</sup>

Yingda Cheng<sup>2</sup>, Irene M. Gamba<sup>3</sup>

Department of Mathematics and ICES, University of Texas, Austin, TX 78712

Armando Majorana<sup>4</sup>

Dipartimento di Matematica e Informatica, Università di Catania, Catania, Italy

*and*

Chi-Wang Shu<sup>5</sup>

Division of Applied Mathematics, Brown University, Providence, RI 02912

## Abstract

In this paper, we present results of a discontinuous Galerkin (DG) scheme applied to deterministic computations of the transients for the Boltzmann-Poisson system describing electron transport in semiconductor devices. The collisional term models optical-phonon interactions which become dominant under strong energetic conditions corresponding to nano-scale active regions under applied bias. The proposed numerical technique is a finite element method using discontinuous piecewise polynomials as basis functions on unstructured meshes. It is applied to simulate hot electron transport in bulk silicon, in a silicon  $n^+ - n - n^+$  diode and in a double gated 12nm MOSFET. Additionally, the obtained results are compared

---

<sup>1</sup>Support from the Institute of Computational Engineering and Sciences and the University of Texas Austin is gratefully acknowledged.

<sup>2</sup>E-mail: ycheng@math.utexas.edu.

<sup>3</sup>E-mail: gamba@math.utexas.edu. Research supported by NSF-0807712 and NSF-FRG-0757450.

<sup>4</sup>E-mail: majorana@dmi.unict.it. Research supported by Italian PRIN 2006: Kinetic and continuum models for particle transport in gases and semiconductors: analytical and computational aspects.

<sup>5</sup>E-mail: shu@dam.brown.edu. Research supported by NSF grant DMS-0809086 and DOE grant DE-FG02-08ER25863.

to those of a high order WENO scheme simulation and DSMC (Discrete Simulation Monte Carlo) solvers.

**Keywords:** Deterministic numerical methods, Discontinuous Galerkin schemes, Boltzmann Poisson systems, Statistical hot electron transport, Semiconductor nano scale devices.

# 1 Introduction

The evolution of the electron distribution function  $f(t, \mathbf{x}, \mathbf{k})$  in semiconductors in dependence of time  $t$ , position  $\mathbf{x}$  and electron wave vector  $\mathbf{k}$  is governed by the Boltzmann transport equation (BTE) [23, 27, 19]

$$\frac{\partial f}{\partial t} + \frac{1}{\hbar} \nabla_{\mathbf{k}} \varepsilon \cdot \nabla_{\mathbf{x}} f - \frac{q}{\hbar} \mathbf{E} \cdot \nabla_{\mathbf{k}} f = Q(f), \quad (1.1)$$

where  $\hbar$  is the reduced Planck constant, and  $q$  denotes the positive elementary charge. The function  $\varepsilon(\mathbf{k})$  is the energy of the considered crystal conduction band measured from the band minimum; according to the Kane dispersion relation,  $\varepsilon$  is the positive root of

$$\varepsilon(1 + \alpha\varepsilon) = \frac{\hbar^2 k^2}{2m^*}, \quad (1.2)$$

where  $\alpha$  is the non-parabolicity factor and  $m^*$  the effective electron mass. The electric field  $\mathbf{E}$  is related to the doping density  $N_D$  and the electron density  $n$ , which equals the zero-order moment of the electron distribution function  $f$ , by the Poisson equation

$$\nabla_{\mathbf{x}} [\varepsilon_r(\mathbf{x}) \nabla_{\mathbf{x}} V] = \frac{q}{\epsilon_0} [n(t, \mathbf{x}) - N_D(\mathbf{x})], \quad \mathbf{E} = -\nabla_{\mathbf{x}} V, \quad (1.3)$$

where  $\epsilon_0$  is the dielectric constant of the vacuum,  $\varepsilon_r(\mathbf{x})$  labels the relative dielectric function depending on the material and  $V$  the electrostatic potential. The collision operator  $Q(f)$  takes into account acoustic deformation potential and optical intervalley scattering [29, 28].

For low electron densities, it reads

$$Q(f)(t, \mathbf{x}, \mathbf{k}) = \int_{\mathbb{R}^3} [S(\mathbf{k}', \mathbf{k})f(t, \mathbf{x}, \mathbf{k}') - S(\mathbf{k}, \mathbf{k}')f(t, \mathbf{x}, \mathbf{k})] d\mathbf{k}' \quad (1.4)$$

with the scattering kernel

$$\begin{aligned} S(\mathbf{k}, \mathbf{k}') &= (n_q + 1) K \delta(\varepsilon(\mathbf{k}') - \varepsilon(\mathbf{k}) + \hbar\omega_p) \\ &\quad + n_q K \delta(\varepsilon(\mathbf{k}') - \varepsilon(\mathbf{k}) - \hbar\omega_p) + K_0 \delta(\varepsilon(\mathbf{k}') - \varepsilon(\mathbf{k})) \end{aligned} \quad (1.5)$$

and  $K$  and  $K_0$  being constant for silicon. The symbol  $\delta$  indicates the usual Dirac distribution and  $\omega_p$  is the constant phonon frequency. Moreover,

$$n_q = \left[ \exp\left(\frac{\hbar\omega_p}{k_B T_L}\right) - 1 \right]^{-1}$$

is the occupation number of phonons,  $k_B$  is the Boltzmann constant and  $T_L$  is the constant lattice temperature.

Semiclassical description of electron flow in semiconductors thus is an equation in six dimensions (plus time if the device is not in steady state) for a truly 3-D device, and four dimensions for a 1-D device. This heavy computational cost explains why the BP system is traditionally simulated by the Direct Simulation Monte Carlo (DSMC) methods [22]. In recent years, deterministic solvers to the BP system were proposed [18, 26, 3, 2, 4, 5, 6, 20]. These methods provide accurate results which, in general, agree well with those obtained from Monte Carlo (DSMC) simulations, often at a fractional computational time. Moreover, they can resolve transient details for the *pdf*, which are difficult to compute with DSMC simulators. The methods proposed in [4, 6] used weighted essentially non-oscillatory (WENO) finite difference schemes to solve the Boltzmann-Poisson system. The advantage of the WENO scheme is that it is relatively simple to code and very stable even on coarse meshes for solutions containing sharp gradient regions. A disadvantage of the WENO finite difference method is that it requires smooth meshes to achieve high order accuracy, hence it is not very flexible for adaptive meshes.

On the other hand, motivated by the easy *hp*-adaptivity and simple communication pattern of the discontinuous Galerkin (DG) methods, researchers have worked on developing the DG method for solving the Boltzmann equation and its macroscopic models [7, 8, 24, 25, 21]. The type of DG method that we will discuss here is a class of finite element methods originally devised to solve hyperbolic conservation laws containing only first order spatial derivatives, e.g. [14, 13, 12, 11, 15]. Using completely discontinuous polynomial space for both the test and trial functions in the spatial variables and coupled with explicit and nonlinearly stable high order Runge-Kutta time discretization, the method has the advantage of flexibility for arbitrarily unstructured meshes, with a compact stencil, and with the ability to easily accommodate arbitrary *hp*-adaptivity. For more details about DG scheme for convection dominated problems, we refer to the review paper [17]. The

DG method was later generalized to the local DG (LDG) method to solve the convection diffusion equation [16] and elliptic equations [1]. It is  $L^2$  stable and locally conservative, which makes it particularly suitable to treat the Poisson equation. In our previous work [10, 9], we proposed the first DG solver for (1.1) and showed some preliminary numerical calculations for one- and two-dimensional devices. In this paper, we will carefully formulate the DG-LDG scheme for the Boltzmann-Poisson system and perform extensive numerical studies to validate our calculation.

This paper is organized as follows: in Section 2, we review the change of variables in [26, 5]. In Section 3, we study the DG-BTE solver for 1D diodes. Section 4 is devoted to the discussion of the 2D double gate MOSFET DG solver. Conclusions and final remarks are presented in Section 5. Some technical implementations of the DG solver are collected in the Appendix.

## 2 Change of variables

In this section, we review the change of variables proposed in [26, 4].

For the numerical treatment of the system (1.1), (1.3), it is convenient to introduce suitable dimensionless quantities and variables. We assume  $T_L = 300 K$ . Typical values for length, time and voltage are  $\ell_* = 10^{-6} m$ ,  $t_* = 10^{-12} s$  and  $V_* = 1 \text{ Volt}$ , respectively. Thus, we define the dimensionless variables

$$(x, y, z) = \frac{\mathbf{x}}{\ell_*}, \quad t = \frac{t}{t_*}, \quad \Psi = \frac{V}{V_*}, \quad (E_x, E_y, E_z) = \frac{\mathbf{E}}{E_*}$$

with  $E_* = 0.1 V_* \ell_*^{-1}$  and

$$E_x = -c_v \frac{\partial \Psi}{\partial x}, \quad E_y = -c_v \frac{\partial \Psi}{\partial y}, \quad c_v = \frac{V_*}{\ell_* E_*}.$$

In correspondence to [26] and [5], we perform a coordinate transformation for  $\mathbf{k}$  according to

$$\mathbf{k} = \frac{\sqrt{2m^*k_B T_L}}{\hbar} \sqrt{w(1 + \alpha_K w)} \left( \mu, \sqrt{1 - \mu^2} \cos \varphi, \sqrt{1 - \mu^2} \sin \varphi \right), \quad (2.6)$$

where the new independent variables are the dimensionless energy  $w = \frac{\varepsilon}{k_B T_L}$ , the cosine of the polar angle  $\mu$  and the azimuth angle  $\varphi$  with  $\alpha_K = k_B T_L \alpha$ . The main advantage of the generalized spherical coordinates (2.6) is the easy treatment of the Dirac distribution in the kernel (1.5) of the collision term. In fact, this procedure enables us to transform the integral operator (1.4) with the nonregular kernel  $S$  into an integral-difference operator, as shown in the following.

We are interested in studying two-dimensional problems in real space but, of course, in the whole three-dimensional  $\mathbf{k}$ -space. Therefore, it is useful to consider the new unknown function  $\Phi$  related to the electron distribution function via

$$\Phi(t, x, y, w, \mu, \varphi) = s(w)f(t, \mathbf{x}, \mathbf{k}),$$

where

$$s(w) = \sqrt{w(1 + \alpha_K w)}(1 + 2\alpha_K w), \quad (2.7)$$

is proportional to the Jacobian of the change of variables (2.6) and, apart from a dimensional constant factor, to the density of states. This allows us to write the free streaming operator of the dimensionless Boltzmann equation in a conservative form, which is appropriate for applying standard numerical schemes used for hyperbolic partial differential equations. Due to the symmetry of the problem and of the collision operator, we have

$$\Phi(t, x, y, w, \mu, 2\pi - \varphi) = \Phi(t, x, y, w, \mu, \varphi). \quad (2.8)$$

Straightforward but cumbersome calculations end in the following transport equation for  $\Phi$ :

$$\frac{\partial \Phi}{\partial t} + \frac{\partial}{\partial x}(g_1 \Phi) + \frac{\partial}{\partial y}(g_2 \Phi) + \frac{\partial}{\partial w}(g_3 \Phi) + \frac{\partial}{\partial \mu}(g_4 \Phi) + \frac{\partial}{\partial \varphi}(g_5 \Phi) = C(\Phi). \quad (2.9)$$

The functions  $g_i$  ( $i = 1, 2, \dots, 5$ ) in the advection terms depend on the independent variables

$w, \mu, \varphi$  as well as on time and position via the electric field. They are given by

$$\begin{aligned}
g_1(\cdot) &= c_x \frac{\mu \sqrt{w(1 + \alpha_K w)}}{1 + 2\alpha_K w}, \\
g_2(\cdot) &= c_x \frac{\sqrt{1 - \mu^2} \sqrt{w(1 + \alpha_K w)} \cos \varphi}{1 + 2\alpha_K w}, \\
g_3(\cdot) &= -2c_k \frac{\sqrt{w(1 + \alpha_K w)}}{1 + 2\alpha_K w} \left[ \mu E_x(t, x, y) + \sqrt{1 - \mu^2} \cos \varphi E_y(t, x, y) \right], \\
g_4(\cdot) &= -c_k \frac{\sqrt{1 - \mu^2}}{\sqrt{w(1 + \alpha_K w)}} \left[ \sqrt{1 - \mu^2} E_x(t, x, y) - \mu \cos \varphi E_y(t, x, y) \right], \\
g_5(\cdot) &= c_k \frac{\sin \varphi}{\sqrt{w(1 + \alpha_K w)} \sqrt{1 - \mu^2}} E_y(t, x, y)
\end{aligned}$$

with

$$c_x = \frac{t_*}{\ell_*} \sqrt{\frac{2k_B T_L}{m^*}} \quad \text{and} \quad c_k = \frac{t_* q E_*}{\sqrt{2m^* k_B T_L}}.$$

The right hand side of (2.9) is the integral-difference operator

$$\begin{aligned}
C(\Phi)(t, x, y, w, \mu, \varphi) &= s(w) \left\{ c_0 \int_0^\pi d\varphi' \int_{-1}^1 d\mu' \Phi(t, x, y, w, \mu', \varphi') \right. \\
&+ \left. \int_0^\pi d\varphi' \int_{-1}^1 d\mu' [c_+ \Phi(t, x, y, w + \gamma, \mu', \varphi') + c_- \Phi(t, x, y, w - \gamma, \mu', \varphi')] \right\} \\
&- 2\pi [c_0 s(w) + c_+ s(w - \gamma) + c_- s(w + \gamma)] \Phi(t, x, y, w, \mu, \varphi),
\end{aligned}$$

where

$$(c_0, c_+, c_-) = \frac{2m^* t_*}{\hbar^3} \sqrt{2m^* k_B T_L} (K_0, (n_q + 1)K, n_q K), \quad \gamma = \frac{\hbar \omega_p}{k_B T_L}$$

are dimensionless parameters. We remark that the  $\delta$  distributions in the kernel  $S$  have been eliminated which leads to the shifted arguments of  $\Phi$ . The parameter  $\gamma$  represents the jump constant corresponding to the quantum of energy  $\hbar \omega_p$ . We have also taken into account (2.8) in the integration with respect to  $\varphi'$ . Since the energy variable  $\omega$  is not negative, we must consider null  $\Phi$  and the function  $s$ , if the argument  $\omega - \gamma$  is negative.

In terms of the new variables the electron density becomes

$$n(t_* t, \ell_* x, \ell_* y) = \int_{\mathbb{R}^3} f(t_* t, \ell_* x, \ell_* y, \mathbf{k}) d\mathbf{k} = \left( \frac{\sqrt{2m^* k_B T_L}}{\hbar} \right)^3 \rho(t, x, y),$$

where

$$\rho(t, x, y) = \int_0^{+\infty} dw \int_{-1}^1 d\mu \int_0^\pi d\varphi \Phi(t, x, y, w, \mu, \varphi). \quad (2.10)$$

Hence, the dimensionless Poisson equation writes

$$\frac{\partial}{\partial x} \left( \epsilon_r \frac{\partial \Psi}{\partial x} \right) + \frac{\partial}{\partial y} \left( \epsilon_r \frac{\partial \Psi}{\partial y} \right) = c_p [\rho(t, x, y) - \mathcal{N}_D(x, y)] \quad (2.11)$$

with

$$\mathcal{N}_D(x, y) = \left( \frac{\sqrt{2 m^* k_B T_L}}{\hbar} \right)^{-3} N_D(\ell_* x, \ell_* y) \quad \text{and} \quad c_p = \left( \frac{\sqrt{2 m^* k_B T_L}}{\hbar} \right)^3 \frac{\ell_*^2 q}{\epsilon_0}.$$

Choosing the same values of the physical parameters as in [26], we obtain

$c_0 \approx 0.26531$	$c_x \approx 0.16857$	$c_p \approx 1830349.$
$c_+ \approx 0.50705$	$c_k \approx 0.32606$	$c_v = 10.$
$c_- \approx 0.04432$	$\gamma \approx 2.43723$	$\alpha_K \approx 0.01292$
$\epsilon_r = 11.7$		

Moreover, the dimensional  $x$ -component of the velocity is given by

$$\frac{\int_0^{+\infty} dw \int_{-1}^1 d\mu \int_0^\pi d\varphi g_1(w, \mu) \Phi(t, x, y, w, \mu, \varphi)}{\rho(t, x, y)},$$

the dimensional density by

$$1.0115 \times 10^{26} \times \rho(t, x, y),$$

and the energy by

$$0.025849 \times \frac{\int_0^{+\infty} dw \int_{-1}^1 d\mu \int_0^\pi d\varphi w \Phi(t, x, y, w, \mu, \varphi)}{\rho(t, x, y)}.$$

In some simplified models, we consider our device in the  $x$ -direction by assuming that the doping profile, the potential and thus the force field are only  $x$ -dependent. By cylindrical symmetry, the resulting distribution function does not depend on  $\varphi$ . In this case, the Boltzmann transport equation is reduced to

$$\frac{\partial \Phi}{\partial t} + \frac{\partial}{\partial x}(g_1 \Phi) + \frac{\partial}{\partial w}(g_3 \Phi) + \frac{\partial}{\partial \mu}(g_4 \Phi) = C(\Phi). \quad (2.12)$$



with

$$\begin{aligned}
g_1(\cdot) &= c_x \frac{\mu \sqrt{w(1 + \alpha_K w)}}{1 + 2\alpha_K w}, \\
g_3(\cdot) &= -2c_k \frac{\sqrt{w(1 + \alpha_K w)}}{1 + 2\alpha_K w} \mu E(t, x), \\
g_4(\cdot) &= -c_k \frac{1 - \mu^2}{\sqrt{w(1 + \alpha_K w)}} E(t, x)
\end{aligned}$$

and

$$\begin{aligned}
C(\Phi)(t, x, w, \mu) &= s(w) \left\{ c_0 \pi \int_{-1}^1 d\mu' \Phi(t, x, w, \mu') \right. \\
&+ \pi \int_{-1}^1 d\mu' [c_+ \Phi(t, x, w + \gamma, \mu') + c_- \Phi(t, x, w - \gamma, \mu')] \left. \right\} \\
&- 2\pi [c_0 s(w) + c_+ s(w - \gamma) + c_- s(w + \gamma)] \Phi(t, x, w, \mu),
\end{aligned}$$

In terms of the new variables the electron density becomes

$$n(t_* t, \ell_* x) = \int_{\mathbb{R}^3} f(t_* t, \ell_* x, \mathbf{k}) d\mathbf{k} = \left( \frac{\sqrt{2 m^* k_B T_L}}{\hbar} \right)^3 \rho(t, x),$$

where

$$\rho(t, x) = \pi \int_0^{+\infty} dw \int_{-1}^1 d\mu \Phi(t, x, w, \mu). \quad (2.13)$$

Hence, the dimensionless Poisson equation writes

$$\frac{\partial}{\partial x} \left( \epsilon_r \frac{\partial \Psi}{\partial x} \right) = c_p [\rho(t, x) - \mathcal{N}_D(x)] \quad (2.14)$$

and

$$E = -c_v \frac{\partial \Psi}{\partial x}.$$

### 3 DG-BTE solver for 1D diodes simulation

We begin with formulating the DG-BTE solver for 1D diodes. These examples have been thoroughly studied and tested by WENO in [4].

The Boltzmann-Poisson system (2.12) and (2.14) will be solved on the domain

$$x \in [0, L], \quad w \in [0, w_{\max}], \quad \mu \in [-1, 1],$$

where  $L$  is the dimensionless length of the device and  $w_{\max}$  is the maximum value of the energy, which is adjusted in the numerical experiments such that

$$\Phi(t, x, w, \mu) \approx 0 \quad \text{for } w \geq w_{\max} \quad \text{and every } t, x, \mu.$$

In (2.12),  $g_1$  and  $g_3$  are completely smooth in the variable  $w$  and  $\mu$ , assuming  $E$  is given and smooth. However,  $g_4$  is singular for the energy  $w = 0$ , although it is compensated by the  $s(w)$  factor in the definition of  $\Phi$ .

The initial value of  $f$  is a locally Maxwellian distribution at the temperature  $T_L$ ,

$$\Phi(0, x, w, \mu) = s(w)N_D(x)e^{-w}\mathcal{M}$$

with the numerical parameter  $\mathcal{M}$  chosen so that the initial value for the density is equal to the doping  $N_D(x)$ .

We choose to perform our calculations on the following rectangular grid,

$$\Omega_{ikm} = \left[ x_{i-\frac{1}{2}}, x_{i+\frac{1}{2}} \right] \times \left[ w_{k-\frac{1}{2}}, w_{k+\frac{1}{2}} \right] \times \left[ \mu_{m-\frac{1}{2}}, \mu_{m+\frac{1}{2}} \right] \quad (3.15)$$

where  $i = 1, \dots, N_x$ ,  $k = 1, \dots, N_w$ ,  $m = 1, \dots, N_\mu$ , and

$$x_{i\pm\frac{1}{2}} = x_i \pm \frac{\Delta x_i}{2}, \quad w_{k\pm\frac{1}{2}} = w_k \pm \frac{\Delta w_k}{2}, \quad \mu_{m\pm\frac{1}{2}} = \mu_m \pm \frac{\Delta \mu_m}{2}.$$

It is useful that we pick  $N_\mu$  to be even, so the function  $g_1$  will assume a constant sign in each cell  $\Omega_{ikm}$ .

The approximation space is thus defined as

$$V_h^\ell = \{v : v|_{\Omega_{ikm}} \in P^\ell(\Omega_{ikm})\}, \quad (3.16)$$

where  $P^\ell(\Omega_{ikm})$  is the set of all polynomials of degree at most  $\ell$  on  $\Omega_{ikm}$ . The DG formulation for the Boltzmann equation (2.12) would be: to find  $\Phi_h \in V_h^\ell$ , such that

$$\begin{aligned} & \int_{\Omega_{ikm}} (\Phi_h)_t v_h d\Omega - \int_{\Omega_{ikm}} g_1 \Phi_h (v_h)_x d\Omega - \int_{\Omega_{ikm}} g_3 \Phi_h (v_h)_w d\Omega \\ & - \int_{\Omega_{ikm}} g_4 \Phi_h (v_h)_\mu d\Omega + F_x^+ - F_x^- + F_w^+ - F_w^- + F_\mu^+ - F_\mu^- \\ & = \int_{\Omega_{ikm}} C(\Phi_h) v_h d\Omega. \end{aligned} \quad (3.17)$$

for any test function  $v_h \in V_h^\ell$ . In (3.17),

$$F_x^+ = \int_{w_{k-\frac{1}{2}}}^{w_{k+\frac{1}{2}}} \int_{\mu_{m-\frac{1}{2}}}^{\mu_{m+\frac{1}{2}}} g_1 \check{\Phi} v_h^-(x_{i+\frac{1}{2}}, w, \mu) dw d\mu,$$

$$F_x^- = \int_{w_{k-\frac{1}{2}}}^{w_{k+\frac{1}{2}}} \int_{\mu_{m-\frac{1}{2}}}^{\mu_{m+\frac{1}{2}}} g_1 \check{\Phi} v_h^+(x_{i-\frac{1}{2}}, w, \mu) dw d\mu,$$

$$F_w^+ = \int_{x_{i-\frac{1}{2}}}^{x_{i+\frac{1}{2}}} \int_{\mu_{m-\frac{1}{2}}}^{\mu_{m+\frac{1}{2}}} g_3 \hat{\Phi} v_h^-(x, w_{k+\frac{1}{2}}, \mu) dx d\mu,$$

$$F_w^- = \int_{x_{i-\frac{1}{2}}}^{x_{i+\frac{1}{2}}} \int_{\mu_{m-\frac{1}{2}}}^{\mu_{m+\frac{1}{2}}} g_3 \hat{\Phi} v_h^+(x, w_{k-\frac{1}{2}}, \mu) dx d\mu,$$

$$F_\mu^+ = \int_{x_{i-\frac{1}{2}}}^{x_{i+\frac{1}{2}}} \int_{w_{k-\frac{1}{2}}}^{w_{k+\frac{1}{2}}} g_4 \tilde{\Phi} v_h^-(x, w, \mu_{m+\frac{1}{2}}) dx dw,$$

$$F_\mu^- = \int_{x_{i-\frac{1}{2}}}^{x_{i+\frac{1}{2}}} \int_{w_{k-\frac{1}{2}}}^{w_{k+\frac{1}{2}}} g_4 \tilde{\Phi} v_h^+(x, w, \mu_{m-\frac{1}{2}}) dx dw,$$

where the upwind numerical fluxes  $\check{\Phi}$ ,  $\hat{\Phi}$ ,  $\tilde{\Phi}$  are chosen according to the following rules,

- The sign of  $g_1$  only depends on  $\mu$ , if  $\mu_m > 0$ ,  $\check{\Phi} = \Phi^-$ ; otherwise,  $\check{\Phi} = \Phi^+$ .
- The sign of  $g_3$  only depends on  $\mu E(t, x)$ , if  $\mu_m E(t, x_i) < 0$ ,  $\hat{\Phi} = \Phi^-$ ; otherwise,  $\hat{\Phi} = \Phi^+$ .
- The sign of  $g_4$  only depends on  $E(t, x)$ , if  $E(t, x_i) < 0$ ,  $\tilde{\Phi} = \Phi^-$ ; otherwise,  $\tilde{\Phi} = \Phi^+$ .

At the source and drain contacts, we implement the same boundary condition as proposed in [6] to realize neutral charges. In the  $(w, \mu)$ -space, non boundary condition is necessary, since

- at  $w = 0$ ,  $g_3 = 0$ . At  $w = w_{\max}$ ,  $\Phi$  is machine zero.
- At  $\mu = \pm 1$ ,  $g_4 = 0$ ,

$F_w^+$ ,  $F_w^-$ ,  $F_\mu^+$ ,  $F_\mu^-$  are always zero. This saves us the effort of constructing ghost elements in comparison with WENO.

The Poisson equation (2.14) is solved by the LDG method on a consistent grid of (3.15) in the  $x$ -direction. It involves rewriting the equation into the following form,

$$\begin{cases} q = \frac{\partial \Psi}{\partial x} \\ \frac{\partial}{\partial x} (\epsilon_r q) = R(t, x) \end{cases} \quad (3.18)$$

where  $R(t, x) = c_p [\rho(t, x) - \mathcal{N}_D(x)]$  is a known function that can be computed at each time step once  $\Phi$  is solved from (3.17), and the coefficient  $\epsilon_r$  here is a constant. The grid we use is  $I_i = [x_{i-\frac{1}{2}}, x_{i+\frac{1}{2}}]$ , with  $i = 1, \dots, N_x$ . The approximation space is

$$W_h^\ell = \{v : v|_{I_i} \in P^\ell(I_i)\},$$

with  $P^\ell(I_i)$  denoting the set of all polynomials of degree at most  $\ell$  on  $I_i$ . The LDG scheme for (3.18) is given by: to find  $q_h, \Psi_h \in V_h^\ell$ , such that

$$\begin{aligned} & \int_{I_i} q_h v_h dx + \int_{I_i} \Psi_h (v_h)_x dx - \hat{\Psi}_h v_h^-(x_{i+\frac{1}{2}}) + \hat{\Psi}_h v_h^+(x_{i-\frac{1}{2}}) = 0, \\ & - \int_{I_i} \epsilon_r q_h (p_h)_x dx + \widehat{\epsilon_r q_h} p_h^-(x_{i+\frac{1}{2}}) - \widehat{\epsilon_r q_h} p_h^+(x_{i-\frac{1}{2}}) = \int_{I_i} R(t, x) p_h dx \end{aligned} \quad (3.19)$$

hold true for any  $v_h, p_h \in W_h^\ell$ . In the above formulation, the flux is chosen as follows,  $\hat{\Psi}_h = \Psi_h^-$ ,  $\widehat{\epsilon_r q_h} = \epsilon_r q_h^+ - [\Psi_h]$ , where  $[\Psi_h] = \Psi_h^+ - \Psi_h^-$ . At  $x = L$  we need to flip the flux to  $\hat{\Psi}_h = \Psi_h^+$ ,  $\widehat{\epsilon_r q_h} = \epsilon_r q_h^- - [\Psi_h]$  to adapt to the Dirichlet boundary conditions. Solving (3.19), we can obtain the numerical approximation of the electric potential  $\Psi_h$  and electric field  $E_h = -c_v q_h$  on each cell  $I_i$ .

To summarize, start with an initial condition for  $\Phi_h$ , the DG-LDG algorithm advances from  $t^n$  to  $t^{n+1}$  in the following steps:

**Step 1** Compute  $\rho_h(t, x) = \pi \int_0^{+\infty} dw \int_{-1}^1 d\mu \Phi_h(t, x, w, \mu)$ .

**Step 2** Use  $\rho_h(t, x)$  to solve from (3.19) the electric field, and compute  $g_i$ ,  $i = 1, 3, 4$ .

**Step 3** Solve (3.17) and get a method of line ODE for  $\Phi_h$ .

**Step 4** Evolve this ODE by proper time stepping from  $t^n$  to  $t^{n+1}$ , if partial time step is necessary, then repeat Step 1 to 3 as needed.

We want to remark that, unlike WENO, the DG formulation above has no restriction on the mesh size. In fact, nonuniform meshes would be more desirable in practice. For small semiconductor devices, it is common to have nonsmooth doping profiles and strong applied electric fields. The nonsmooth doping profile will create a distribution function  $f$  with high densities in some regions but low densities in other regions. Only a nonuniform grid may guarantee accurate results without using a large number of grid points. The strong electric fields give high energy to the charge particles. Hence the distribution function has, for some fixed points in the physical domain, a shape that is very different from the Maxwellian distribution (the equilibrium distribution in the absence of electric field), see for example Figures 3.11 to 3.14. Moreover, taking into account the exponential decay of  $f$  for large value of  $|\mathbf{k}|$ , a nonuniform grid can save us tremendous amount of computational time without sacrificing accuracy of the calculation. In the following simulations, we use a nonuniform mesh and refine locally near the junction of the channel and near  $\mu = 1$  where most of the interesting phenomena happen.

We consider two test examples: Si  $n^+ - n - n^+$  diodes of a total length of 1 and  $0.25\mu\text{m}$ , with 400 and 50nm channels located in the middle of the device, respectively. For the 400nm channel device, the dimensional doping is given by  $N_D = 5 \times 10^{17}\text{cm}^{-3}$  in the  $n^+$  region and  $N_D = 2 \times 10^{15}\text{cm}^{-3}$  in the  $n^-$  region. For the 50nm channel device, the dimensional doping is given by  $N_D = 5 \times 10^{18}\text{cm}^{-3}$  in the  $n^+$  region and  $N_D = 1 \times 10^{15}\text{cm}^{-3}$  in the  $n^-$  region. Both examples were computed by WENO in [5].

In our simulation, we use piecewise linear polynomials, i.e.  $\ell = 1$ , and second-order Runge-Kutta time discretization. The doping  $N_D$  is smoothed in the following way near the channel junctions to obtain non-oscillatory solutions. Suppose  $N_D = N_D^+$  in the  $n^+$  region,  $N_D = N_D^-$  in the  $n^-$  region and the length of the transition region is 2 cells, then the smoothed function is  $(N_D^+ - N_D^-)(1 - y^3)^3 + N_D^-$ , where  $y = (x - x_0 + \Delta x)/(2\Delta x + 10^{-20})$  is the coordinate transformation that makes the transition region  $(x_0 - \Delta x, x_0 + \Delta x)$  varies from 0 to 1 in  $y$ .

The nonuniform mesh we use for 400nm channels is defined as follows. In the  $x$ -direction, if  $x < 0.2$  or  $x > 0.4$ ,  $\Delta x = 0.01$ . In the region  $0.2 < x < 0.4$ ,  $\Delta x = 0.005$ . Thus, the total number of cells in  $x$  direction is 120. In the  $w$ -direction, we use 60 uniform cells. In the  $\mu$ -direction, we use 24 cells, 12 in the region  $\mu < 0.7$ , 12 in  $\mu > 0.7$ . Thus, the grid consists of  $120 \times 60 \times 24$  cells, compared to the WENO grid of  $180 \times 60 \times 24$  uniform cells.

We plot the evolution of density, mean velocity, energy and momentum in Figure 3.1. The solution has already stabilized at  $t = 5.0$  from the momentum plots. The macroscopic quantities at steady state are plotted in Figure 3.2. The results are compared with the WENO calculation. They agree with each other in general, with DG offering more resolution and a higher peak in energy near the junctions. Figures 3.3 and 3.4 show comparisons for the  $pdf$  at transient and steady state. We plot at different position of the device, namely, the left, center and right of the channel. We notice a larger value of  $pdf$  especially at the center of the channel, where the  $pdf$  is no longer Maxwellian. Moreover, at  $t = 0.5$ ,  $x_0 = 0.5$ , the  $pdf$  shows a double hump structure, which is not captured by the WENO solver. All of these advantages come from the fact that we are refining more near  $\mu = 1$ . To have a better idea of the shape of the  $pdf$ , we plot  $\Phi(t = 5.0, x = 0.5)$  in the cartesian coordinates in Figure 3.9. The coordinate  $V1$  in the plot is the momentum parallel to the force field  $k_1$ ,  $V2$  is the modulus of the orthogonal component. The peak is captured very sharply compared to WENO.

The nonuniform mesh we use for 50nm channels is defined as follows. In the  $x$ -direction, near the junctions, in  $0.09 < x < 0.11$  and  $0.14 < x < 0.16$ ,  $\Delta x = 0.001$ ; in center of the channel  $0.11 < x < 0.14$ ,  $\Delta x = 0.005$ ; at everywhere else,  $\Delta x = 0.01$ . Thus, the total number of cells in  $x$  direction is 64. In the  $w$ -direction, we use 60 uniform cells. In the  $\mu$ -direction, we use 20 cells, 10 in the region  $\mu < 0.7$ , 10 in  $\mu > 0.7$ . Thus, the grid consists of  $64 \times 60 \times 20$  cells, compared to the WENO calculation of  $150 \times 120 \times 16$  uniform cells. The evolution and steady state plots are listed in Figures 3.5 to 3.8. The conclusions are similar with 400nm, that we obtain better resolutions near the channel junctions and the peak for

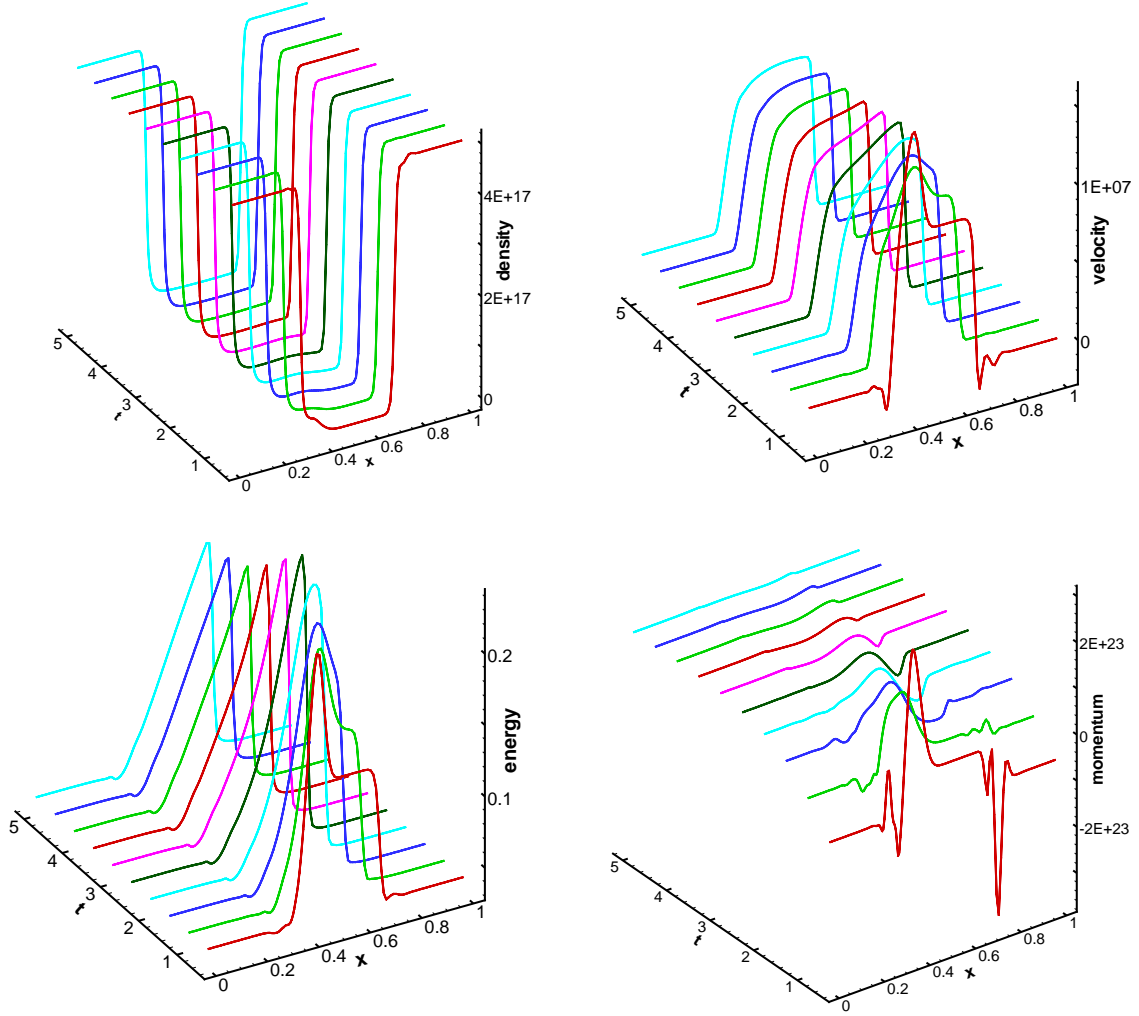


Figure 3.1: Time evolution of macroscopic quantities using DG method for 400nm channel at  $V_{\text{bias}} = 1.0$ . Top left: density in  $\text{cm}^{-3}$ ; top right: mean velocity in  $\text{cm/s}$ ; bottom left: energy in  $\text{eV}$ ; bottom right: momentum in  $\text{cm}^{-2} \text{s}^{-1}$ .

$pdf$  is much higher. Figure 3.10 plots  $\Phi(t = 5.0, x = 0.125)$  in the cartesian coordinates. The peak is twice the height of WENO and is very sharp. Figure 3.11 to 3.14 plot the  $pdf$  near  $x = 0.15$ , the drain junction. We obtain distributions far away from statistical equilibrium, that reflects the lack of suitability of the classical hydrodynamical models for the drain region of a small gated device under even moderate voltage bias.

We also compare the results from DG-BTE solver with those obtained from DSMC simulations, see Figures 3.15, 3.16. The two simulations show good agreement except for energy plots near the boundaries. The modeling of the contact boundaries is not simple,

since it requires to know the distribution function of entering particles. The best way to solve this problem is the inclusion of a transport kinetic equation for the dynamic of the electron at the metal junctions; of course this is not realistic due to the complexity of this new kinetic equation, where the importance of electron-electron interaction requires a nonlinear collisional operator, similar to the classical one of the Boltzmann equation for a rarefied perfect gas. Then, the simplest reasonable rule consists in assuming that the distribution function near, but outside, the device is proportional to a Maxwellian (or shifted Maxwellian) equilibrium distribution function, or to the distribution function near, but inside, the device boundaries. When there are strong electric fields also near the boundaries, the first choice is not reasonable, since, as we show in this paper, the distribution function is very far away to a Maxwellian distribution function. Therefore, the second choice is better than the first. We remark that both choices are simple but only low level approximation of the true physical phenomena; so many criticisms are known in the literature. We assume, as usual, that charge neutrality holds at the contact; so, the particle density near the contact boundaries coincides with the doping density. This law is used in all of the DSMC, WENO and DG simulations. Nevertheless, since we must approximate this constraint in different way, i.e. at molecular level for DSMC, introducing suitable ghost points for WENO scheme or giving appropriate values of  $\Phi$  at boundaries in DG simulations, we cannot have a unique exact boundary condition in the computational experiments. Now, it is obvious that this difference in the boundary treatment has an influence for the solutions at the stationary regime.



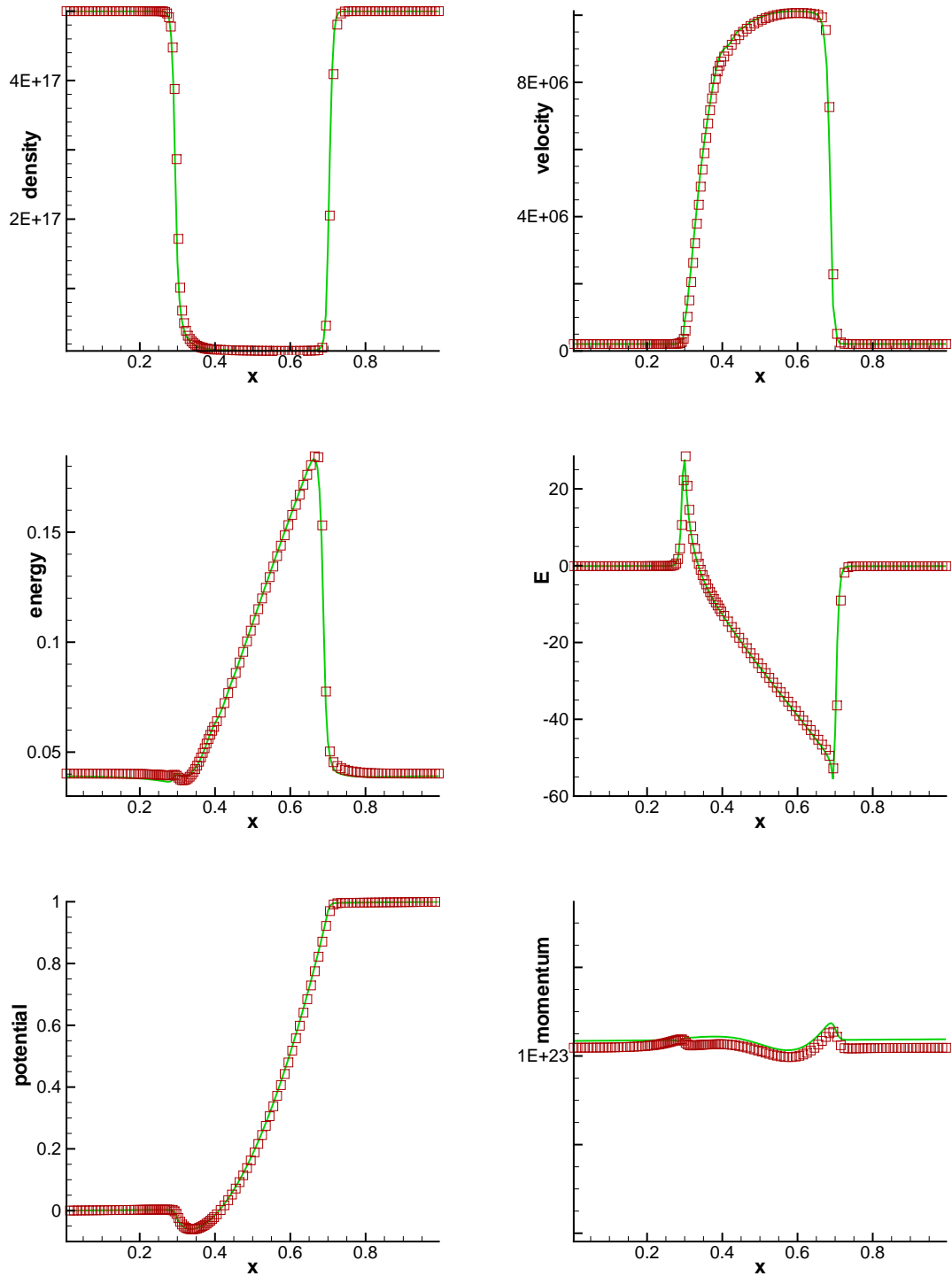


Figure 3.2: Comparison of macroscopic quantities using DG (symbols) and WENO (solid line) for 400nm channel at  $t = 5.0$ ,  $V_{\text{bias}} = 1.0$ . Top left: density in  $\text{cm}^{-3}$ ; top right: mean velocity in  $\text{cm/s}$ ; middle left: energy in  $\text{eV}$ ; middle right: electric field in  $\text{kV/cm}$ ; bottom left: potential in  $\text{V}$ ; bottom right: momentum in  $\text{cm}^{-2} \text{s}^{-1}$ . Solution has reached steady state.

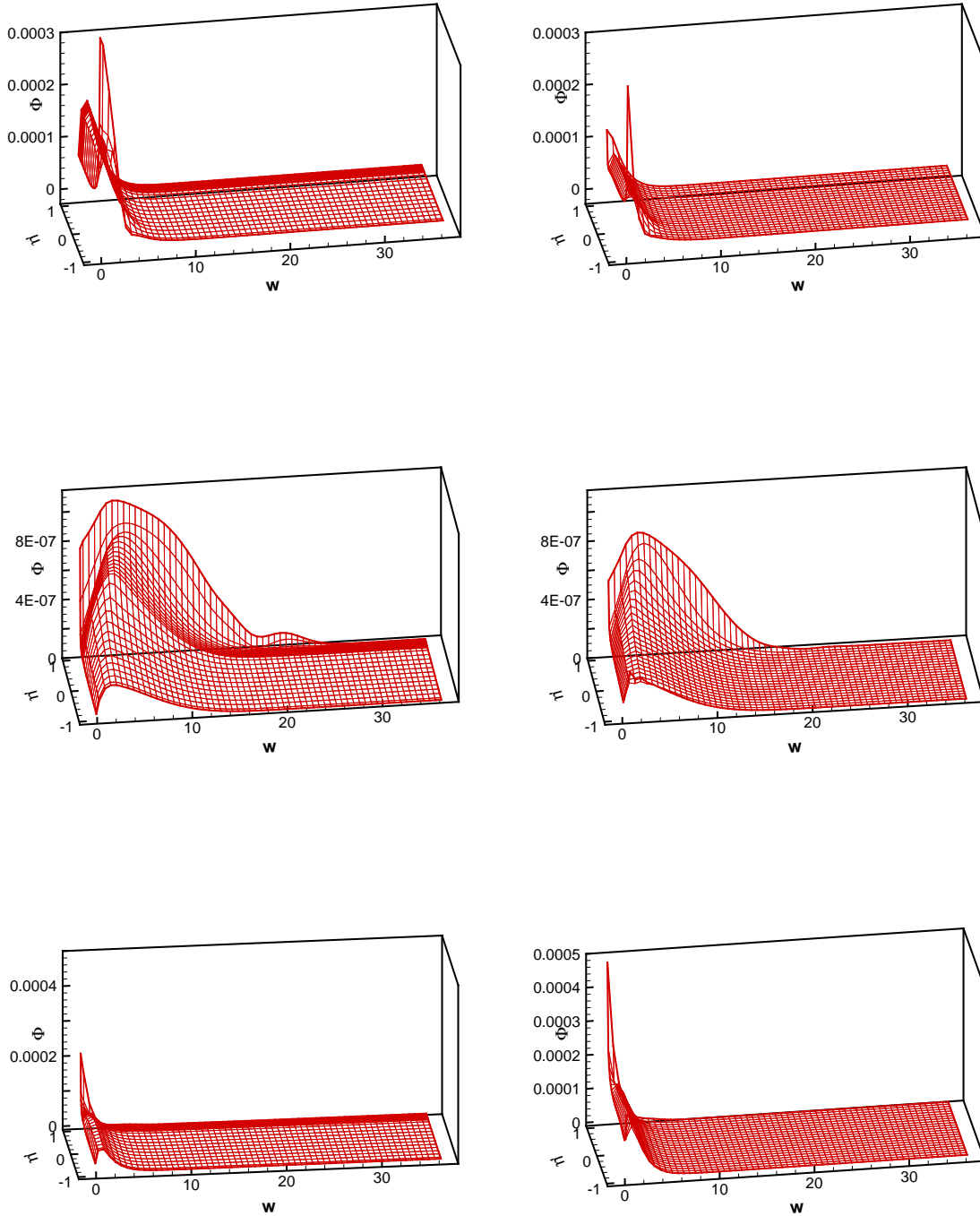


Figure 3.3: Comparison of the snapshot for  $\Phi(x_0, w, \mu)$  using DG (left) and WENO (right) for 400nm channel at  $t = 0.5$ ,  $V_{\text{bias}} = 1.0$ . Top:  $x_0 = 0.3$ ; middle:  $x_0 = 0.5$ ; bottom:  $x_0 = 0.7$ . Solution has not yet reached steady state.

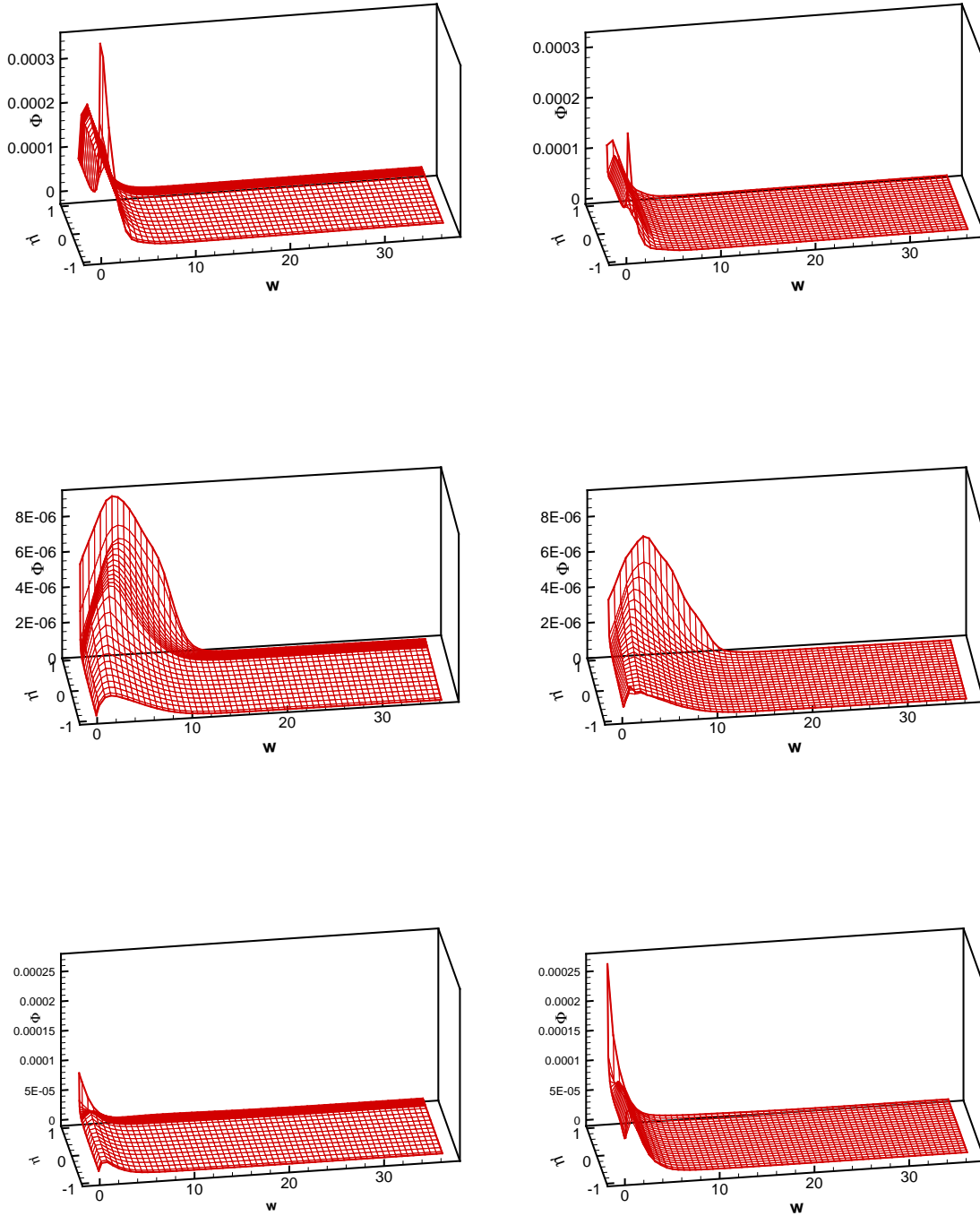


Figure 3.4: Comparison of the snapshot for  $\Phi(x_0, w, \mu)$  using DG (left) and WENO (right) for 400nm channel at  $t = 5.0$ ,  $V_{\text{bias}} = 1.0$ . Top:  $x_0 = 0.3$ ; middle:  $x_0 = 0.5$ ; bottom:  $x_0 = 0.7$ . Solution has reached steady state.

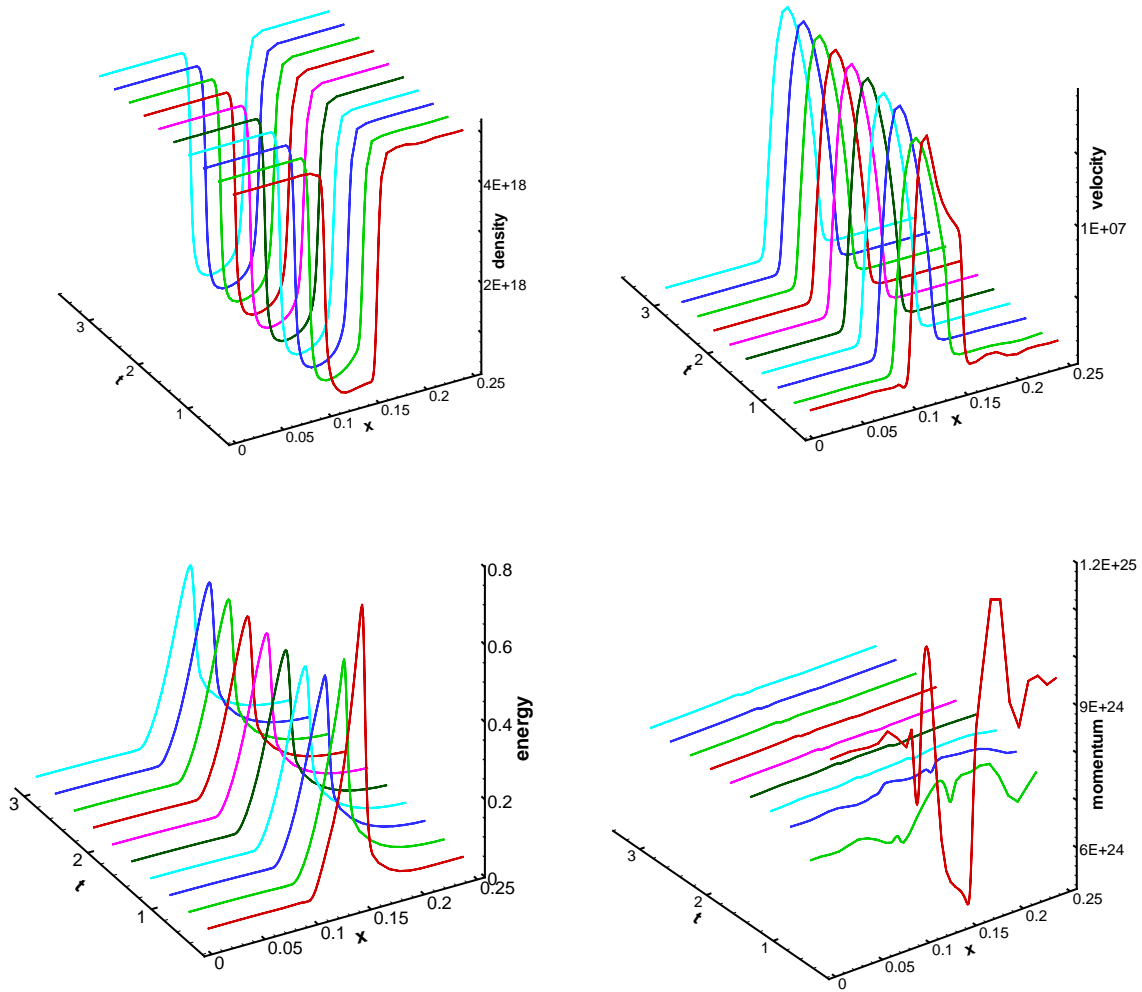


Figure 3.5: Time evolution of macroscopic quantities using DG method for 50nm channel at  $V_{\text{bias}} = 1.0$ . Top left: density in  $\text{cm}^{-3}$ ; top right: mean velocity in  $\text{cm/s}$ ; bottom left: energy in  $\text{eV}$ ; bottom right: momentum in  $\text{cm}^{-2} \text{s}^{-1}$ .

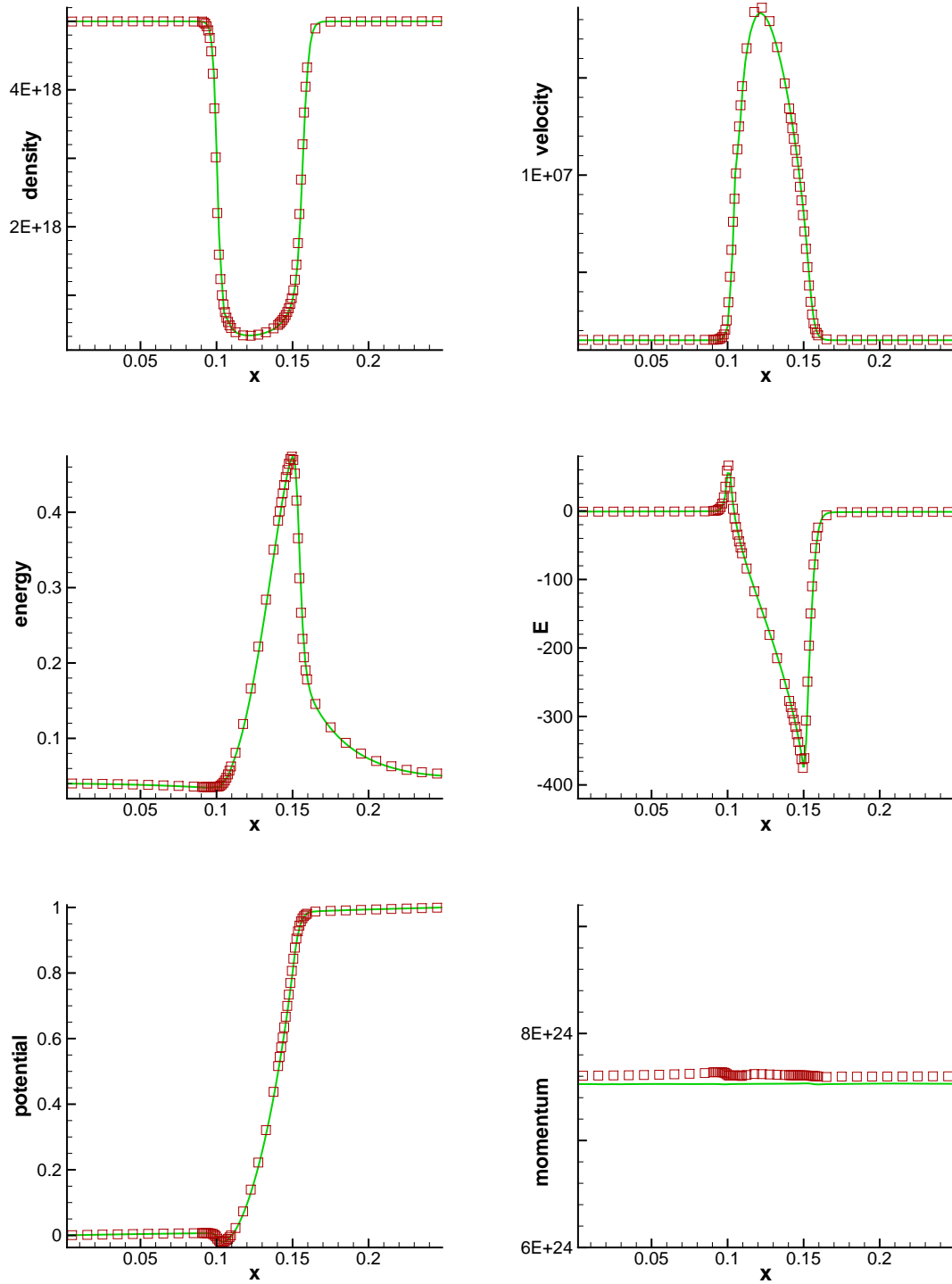


Figure 3.6: Comparison of macroscopic quantities using DG (symbols) and WENO (solid line) for 50nm channel at  $t = 3.0$ ,  $V_{\text{bias}} = 1.0$ . Top left: density in  $\text{cm}^{-3}$ ; top right: mean velocity in  $\text{cm/s}$ ; middle left: energy in  $\text{eV}$ ; middle right: electric field in  $\text{kV/cm}$ ; bottom left: potential in  $\text{V}$ ; bottom right: momentum in  $\text{cm}^{-2} \text{s}^{-1}$ . Solution has reached steady state.

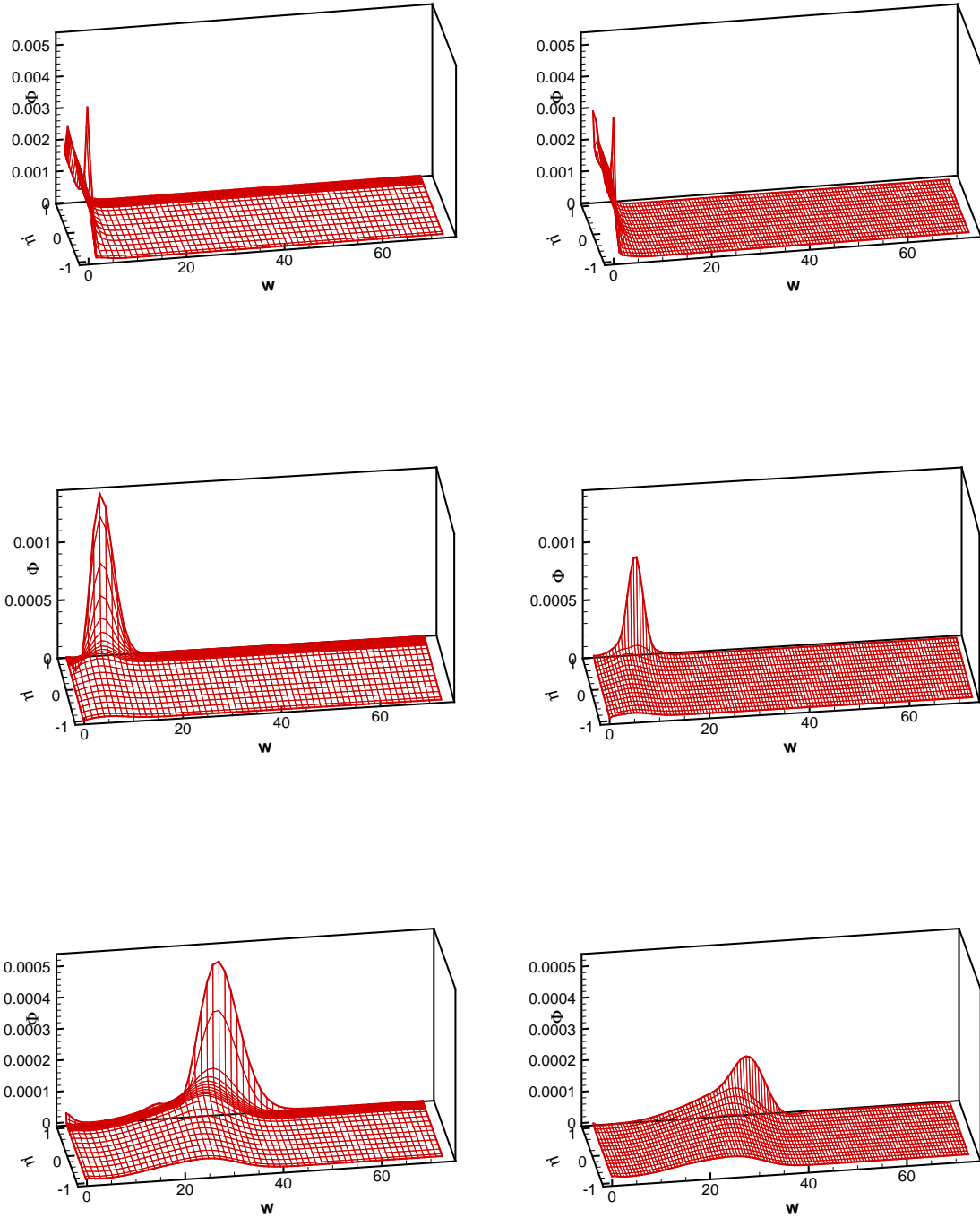


Figure 3.7: Comparison of the snapshot for  $\Phi(x_0, w, \mu)$  using DG (left) and WENO (right) for 50nm channel at  $t = 0.5$ ,  $V_{\text{bias}} = 1.0$ . Top:  $x_0 = 0.1$  ; middle:  $x_0 = 0.125$ ; bottom:  $x_0 = 0.15$ . Solution has not yet reached steady state.

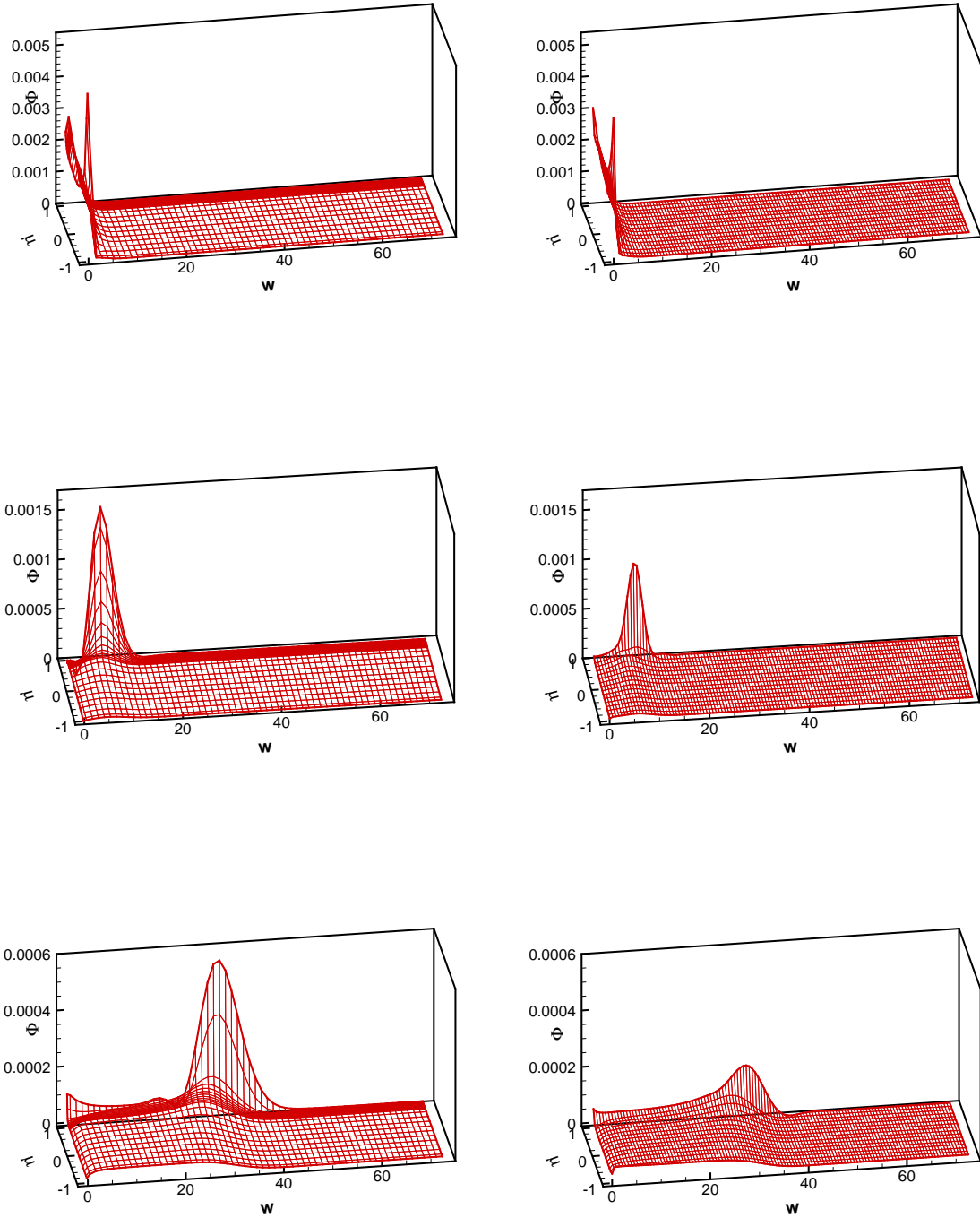


Figure 3.8: Comparison of the snapshot for  $\Phi(x_0, w, \mu)$  using DG (left) and WENO (right) solution for 50nm channel at  $t = 3.0$ ,  $V_{\text{bias}} = 1.0$ . Top:  $x_0 = 0.1$ ; middle:  $x_0 = 0.125$ ; bottom:  $x_0 = 0.15$ . Solution has reached steady state.

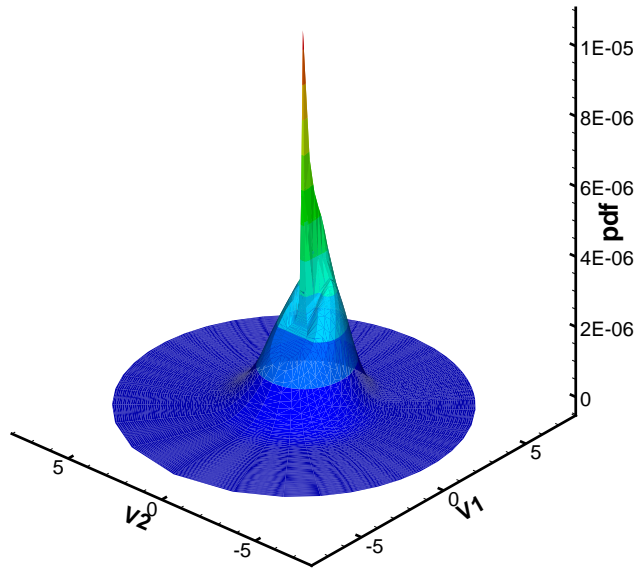


Figure 3.9: PDF for 400nm channel at  $t = 5.0$ ,  $x = 0.5$ .

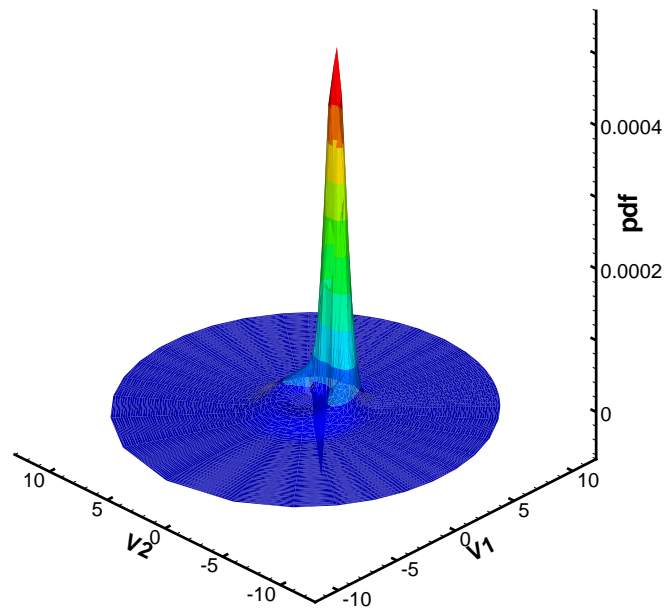


Figure 3.10: PDF for 50nm channel at  $t = 3.0$ ,  $x = 0.125$ .



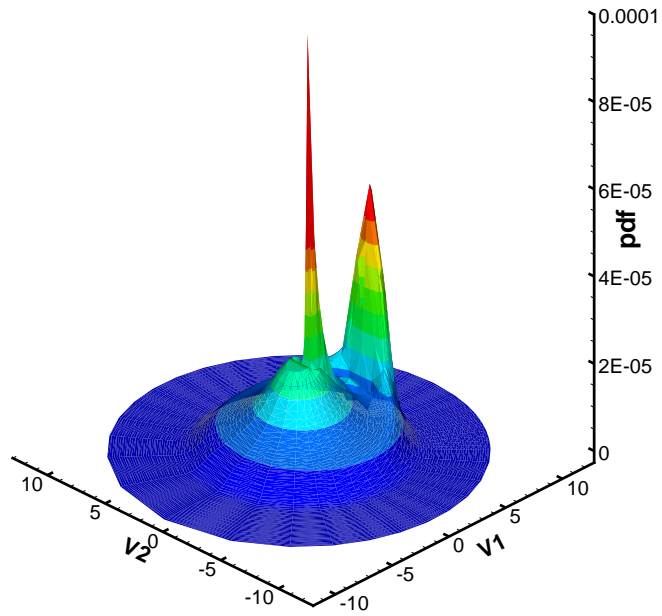


Figure 3.11: PDF for 50nm channel at  $t = 3.0$ ,  $x = 0.149$ .

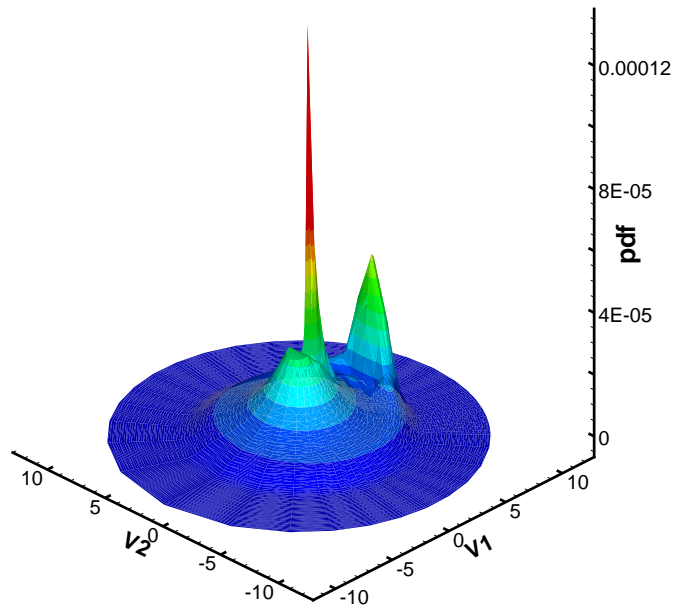


Figure 3.12: PDF for 50nm channel at  $t = 3.0$ ,  $x = 0.15$ .

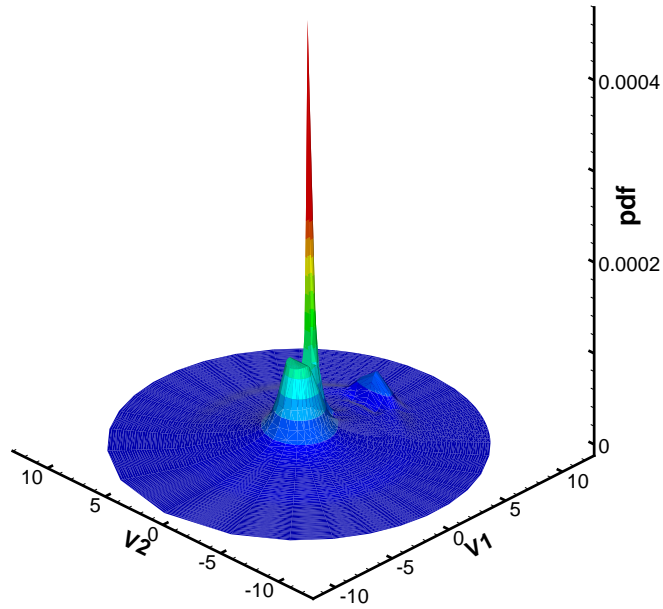


Figure 3.13: PDF for 50nm channel at  $t = 3.0$ ,  $x = 0.152$ .

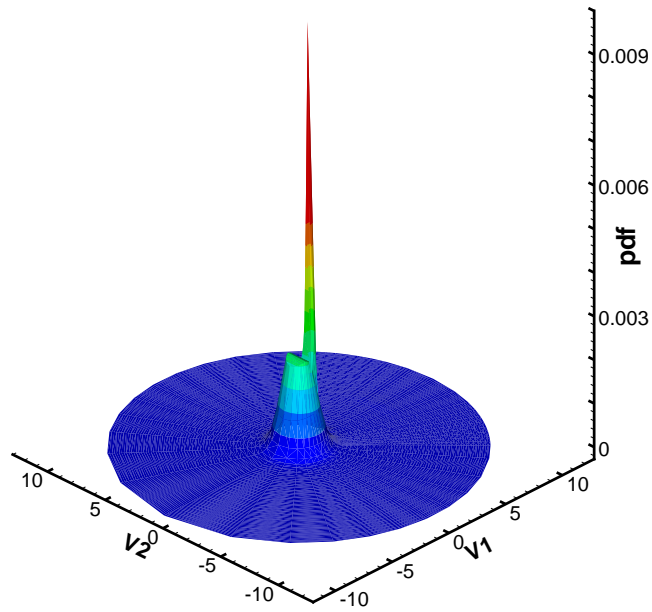


Figure 3.14: PDF for 50nm channel at  $t = 3.0$ ,  $x = 0.16$ .

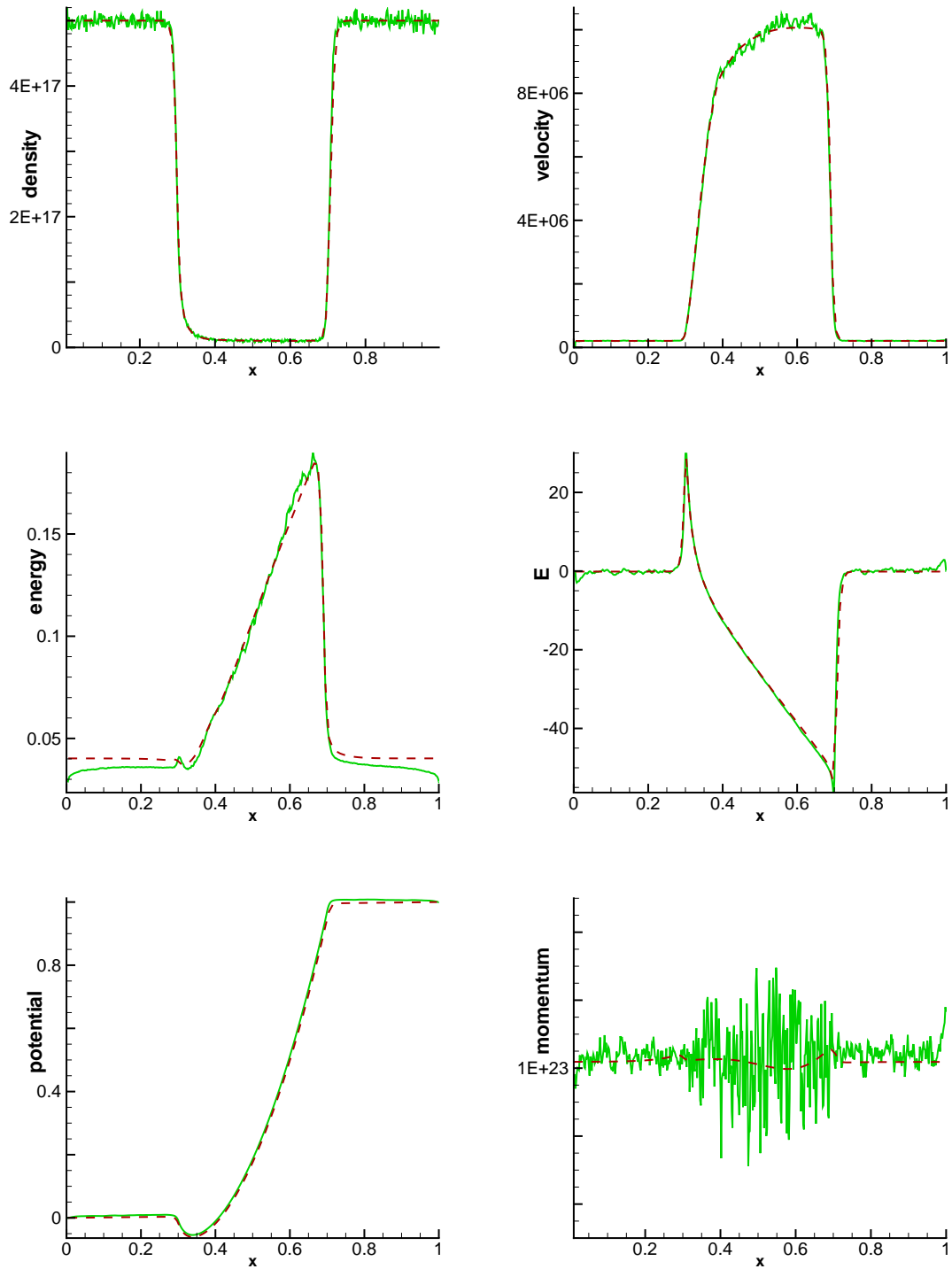


Figure 3.15: Comparison of macroscopic quantities using DG (dashed line) and DSMC (solid line) for 400nm channel at  $t = 5.0$ ,  $V_{\text{bias}} = 1.0$ . Top left: density in  $cm^{-3}$ ; top right: mean velocity in  $cm/s$ ; middle left: energy in  $eV$ ; middle right: electric field in  $kV/cm$ ; bottom left: potential in  $V$ ; bottom right: momentum in  $cm^{-2} s^{-1}$ . Solution has reached steady state.

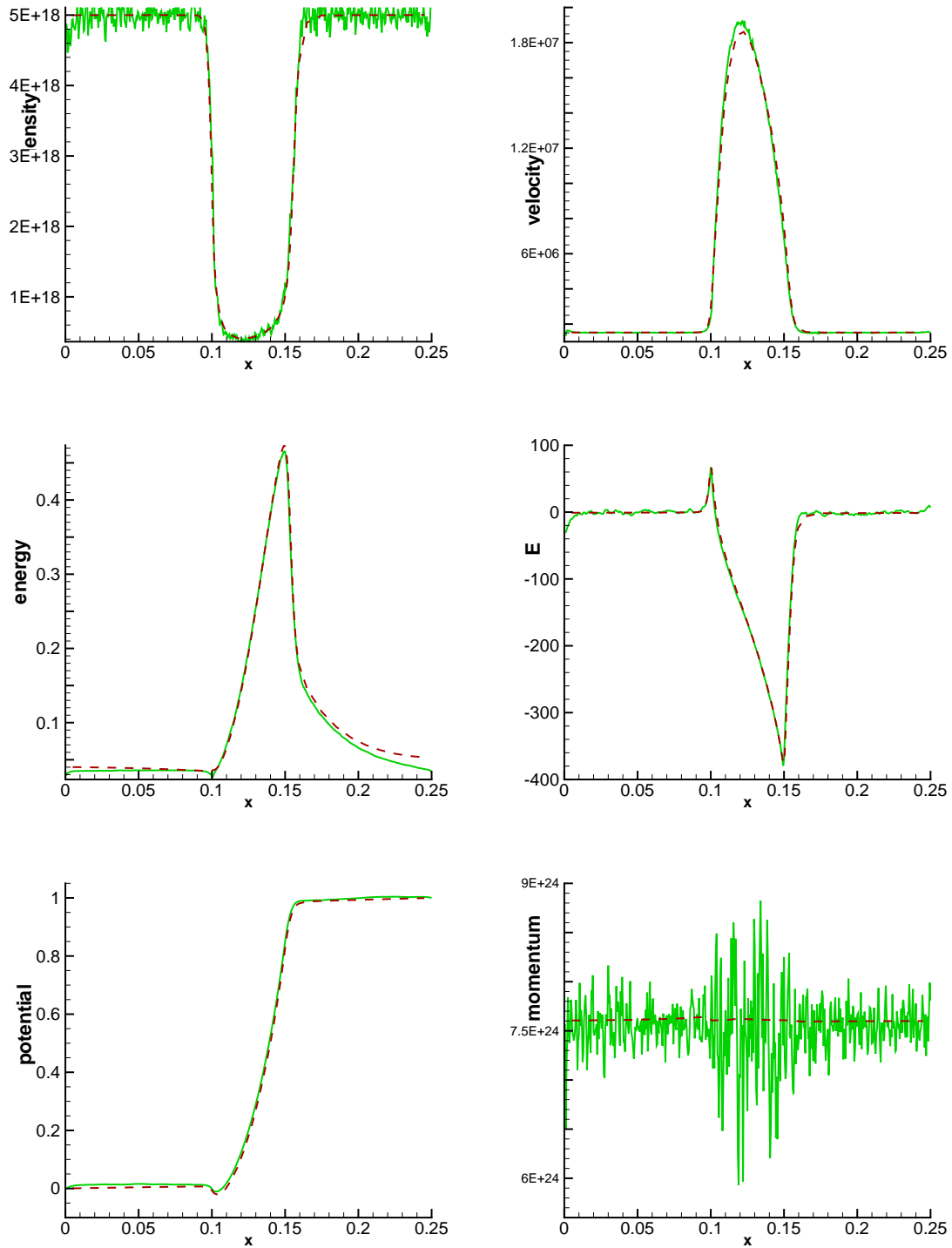


Figure 3.16: Comparison of macroscopic quantities using DG (dashed line) and DSMC (solid line) for 50nm channel at  $t = 3.0$ ,  $V_{\text{bias}} = 1.0$ . Top left: density in  $\text{cm}^{-3}$ ; top right: mean velocity in  $\text{cm/s}$ ; middle left: energy in  $\text{eV}$ ; middle right: electric field in  $\text{kV/cm}$ ; bottom left: potential in  $\text{V}$ ; bottom right: momentum in  $\text{cm}^{-2} \text{s}^{-1}$ . Solution has reached steady state.

## 4 DG-BTE solver for 2D double gate MOSFET simulation

In this section, we consider a 2D double gate MOSFET device. In order to solve the 2D Boltzmann-Poisson system, we choose to implement a simple rectangular grid and let

$$\Omega_{ijkmn} = \left[ x_{i-\frac{1}{2}}, x_{i+\frac{1}{2}} \right] \times \left[ y_{j-\frac{1}{2}}, y_{j+\frac{1}{2}} \right] \times \left[ w_{k-\frac{1}{2}}, w_{k+\frac{1}{2}} \right] \times \left[ \mu_{m-\frac{1}{2}}, \mu_{m+\frac{1}{2}} \right] \times \left[ \varphi_{n-\frac{1}{2}}, \varphi_{n+\frac{1}{2}} \right]$$

where  $i = 1, \dots, N_x$ ,  $j = 1, \dots, N_y$ ,  $k = 1, \dots, N_w$ ,  $m = 1, \dots, N_\mu$ ,  $n = 1, \dots, N_\varphi$ , and

$$x_{i\pm\frac{1}{2}} = x_i \pm \frac{\Delta x_i}{2}, \quad y_{j\pm\frac{1}{2}} = y_j \pm \frac{\Delta y_j}{2}, \quad w_{k\pm\frac{1}{2}} = w_k \pm \frac{\Delta w_k}{2}$$

$$\mu_{m\pm\frac{1}{2}} = \mu_m \pm \frac{\Delta \mu_m}{2}, \quad \varphi_{n\pm\frac{1}{2}} = \varphi_n \pm \frac{\Delta \varphi_n}{2}.$$

The approximation space is defined as

$$V_h^\ell = \{v : v|_{\Omega_{ijkmn}} \in P^\ell(\Omega_{ijkmn})\}. \quad (4.20)$$

Here,  $P^\ell(\Omega_{ijkmn})$  is the set of all polynomials of degree at most  $\ell$  on  $\Omega_{ijkmn}$ . The DG formulation for the Boltzmann equation (2.9) would be: to find  $\Phi_h \in V_h^\ell$ , such that

$$\begin{aligned} & \int_{\Omega_{ijkmn}} (\Phi_h)_t v_h \, d\Omega - \int_{\Omega_{ijkmn}} g_1 \Phi_h (v_h)_x \, d\Omega - \int_{\Omega_{ijkmn}} g_2 \Phi_h (v_h)_y \, d\Omega \\ & - \int_{\Omega_{ijkmn}} g_3 \Phi_h (v_h)_w \, d\Omega - \int_{\Omega_{ijkmn}} g_4 \Phi_h (v_h)_\mu \, d\Omega - \int_{\Omega_{ijkmn}} g_5 \Phi_h (v_h)_\varphi \, d\Omega \\ & + F_x^+ - F_x^- + F_y^+ - F_y^- + F_w^+ - F_w^- + F_\mu^+ - F_\mu^- + F_\varphi^+ - F_\varphi^- = \int_{\Omega_{ijkmn}} C(\Phi_h) v_h \, d\Omega. \end{aligned} \quad (4.21)$$

for any test function  $v_h \in V_h^\ell$ . In (4.21),

$$F_x^+ = \int_{y_{j-\frac{1}{2}}}^{y_{j+\frac{1}{2}}} \int_{w_{k-\frac{1}{2}}}^{w_{k+\frac{1}{2}}} \int_{\mu_{m-\frac{1}{2}}}^{\mu_{m+\frac{1}{2}}} \int_{\varphi_{n-\frac{1}{2}}}^{\varphi_{n+\frac{1}{2}}} g_1 \check{\Phi} v_h^-(x_{i+\frac{1}{2}}, y, w, \mu, \varphi) \, dy \, dw \, d\mu \, d\varphi,$$

$$F_x^- = \int_{y_{j-\frac{1}{2}}}^{y_{j+\frac{1}{2}}} \int_{w_{k-\frac{1}{2}}}^{w_{k+\frac{1}{2}}} \int_{\mu_{m-\frac{1}{2}}}^{\mu_{m+\frac{1}{2}}} \int_{\varphi_{n-\frac{1}{2}}}^{\varphi_{n+\frac{1}{2}}} g_1 \check{\Phi} v_h^+(x_{i-\frac{1}{2}}, y, w, \mu, \varphi) \, dy \, dw \, d\mu \, d\varphi,$$

$$F_y^+ = \int_{x_{i-\frac{1}{2}}}^{x_{i+\frac{1}{2}}} \int_{w_{k-\frac{1}{2}}}^{w_{k+\frac{1}{2}}} \int_{\mu_{m-\frac{1}{2}}}^{\mu_{m+\frac{1}{2}}} \int_{\varphi_{n-\frac{1}{2}}}^{\varphi_{n+\frac{1}{2}}} g_2 \bar{\Phi} v_h^-(x, y_{j+\frac{1}{2}}, w, \mu, \varphi) \, dx \, dw \, d\mu \, d\varphi,$$

$$F_y^- = \int_{x_{i-\frac{1}{2}}}^{x_{i+\frac{1}{2}}} \int_{w_{k-\frac{1}{2}}}^{w_{k+\frac{1}{2}}} \int_{\mu_{m-\frac{1}{2}}}^{\mu_{m+\frac{1}{2}}} \int_{\varphi_{n-\frac{1}{2}}}^{\varphi_{n+\frac{1}{2}}} g_2 \bar{\Phi} v_h^+(x, y_{j-\frac{1}{2}}, w, \mu, \varphi) dx dw d\mu d\varphi,$$

$$F_w^+ = \int_{x_{i-\frac{1}{2}}}^{x_{i+\frac{1}{2}}} \int_{y_{j-\frac{1}{2}}}^{y_{j+\frac{1}{2}}} \int_{\mu_{m-\frac{1}{2}}}^{\mu_{m+\frac{1}{2}}} \int_{\varphi_{n-\frac{1}{2}}}^{\varphi_{n+\frac{1}{2}}} \widehat{g_3 \Phi} v_h^-(x, y, w_{k+\frac{1}{2}}, \mu, \varphi) dx dy d\mu d\varphi,$$

$$F_w^- = \int_{x_{i-\frac{1}{2}}}^{x_{i+\frac{1}{2}}} \int_{y_{j-\frac{1}{2}}}^{y_{j+\frac{1}{2}}} \int_{\mu_{m-\frac{1}{2}}}^{\mu_{m+\frac{1}{2}}} \int_{\varphi_{n-\frac{1}{2}}}^{\varphi_{n+\frac{1}{2}}} \widehat{g_3 \Phi} v_h^+(x, y, w_{k-\frac{1}{2}}, \mu, \varphi) dx dy d\mu d\varphi,$$

$$F_\mu^+ = \int_{x_{i-\frac{1}{2}}}^{x_{i+\frac{1}{2}}} \int_{y_{j-\frac{1}{2}}}^{y_{j+\frac{1}{2}}} \int_{w_{k-\frac{1}{2}}}^{w_{k+\frac{1}{2}}} \int_{\varphi_{n-\frac{1}{2}}}^{\varphi_{n+\frac{1}{2}}} \widetilde{g_4 \Phi} v_h^-(x, y, w, \mu_{m+\frac{1}{2}}, \varphi) dx dy dw d\varphi,$$

$$F_\mu^- = \int_{x_{i-\frac{1}{2}}}^{x_{i+\frac{1}{2}}} \int_{y_{j-\frac{1}{2}}}^{y_{j+\frac{1}{2}}} \int_{w_{k-\frac{1}{2}}}^{w_{k+\frac{1}{2}}} \int_{\varphi_{n-\frac{1}{2}}}^{\varphi_{n+\frac{1}{2}}} \widetilde{g_4 \Phi} v_h^+(x, y, w, \mu_{m-\frac{1}{2}}, \varphi) dx dy dw d\varphi,$$

$$F_\varphi^+ = \int_{x_{i-\frac{1}{2}}}^{x_{i+\frac{1}{2}}} \int_{y_{j-\frac{1}{2}}}^{y_{j+\frac{1}{2}}} \int_{w_{k-\frac{1}{2}}}^{w_{k+\frac{1}{2}}} \int_{\mu_{m-\frac{1}{2}}}^{\mu_{m+\frac{1}{2}}} g_5 \dot{\Phi} v_h^-(x, y, w, \mu, \varphi_{n+\frac{1}{2}}) dx dy dw d\mu,$$

$$F_\varphi^- = \int_{x_{i-\frac{1}{2}}}^{x_{i+\frac{1}{2}}} \int_{y_{j-\frac{1}{2}}}^{y_{j+\frac{1}{2}}} \int_{w_{k-\frac{1}{2}}}^{w_{k+\frac{1}{2}}} \int_{\mu_{m-\frac{1}{2}}}^{\mu_{m+\frac{1}{2}}} g_5 \dot{\Phi} v_h^+(x, y, w, \mu, \varphi_{n-\frac{1}{2}}) dx dy dw d\mu.$$

where the upwind numerical fluxes  $\check{\Phi}$ ,  $\bar{\Phi}$ ,  $\widehat{g_3 \Phi}$ ,  $\widetilde{g_4 \Phi}$ ,  $\dot{\Phi}$  are defined in the following way,

- The sign of  $g_1$  only depends on  $\mu$ , if  $\mu_m > 0$ , then  $\check{\Phi} = \Phi^-$ ; otherwise,  $\check{\Phi} = \Phi^+$ .
- The sign of  $g_2$  only depends on  $\cos \varphi$ , if  $\cos \varphi_n > 0$ , then  $\bar{\Phi} = \Phi^-$ ; otherwise,  $\bar{\Phi} = \Phi^+$ .

Note that in our simulation,  $N_\varphi$  is always even.

- For  $\widehat{g_3 \Phi}$ , we let

$$\widehat{g_3 \Phi} = -2c_k \frac{\sqrt{w(1 + \alpha_K w)}}{1 + 2\alpha_K w} \left[ \mu E_x(t, x, y) \hat{\Phi} + \sqrt{1 - \mu^2} \cos \varphi E_y(t, x, y) \tilde{\Phi} \right],$$

If  $\mu_m E_x(t, x_i, y_j) < 0$ , then  $\hat{\Phi} = \Phi^-$ ; otherwise,  $\hat{\Phi} = \Phi^+$ .

If  $(\cos \varphi_n) E_y(t, x_i, y_j) < 0$ , then  $\tilde{\Phi} = \Phi^-$ ; otherwise,  $\tilde{\Phi} = \Phi^+$ .

- For  $\widetilde{g_4 \Phi}$ , we let

$$\widetilde{g_4 \Phi} = -c_k \frac{\sqrt{1 - \mu^2}}{\sqrt{w(1 + \alpha_K w)}} \left[ \sqrt{1 - \mu^2} E_x(t, x, y) \hat{\Phi} - \mu \cos \varphi E_y(t, x, y) \tilde{\Phi} \right],$$

If  $E_x(t, x_i, y_j) < 0$ , then  $\hat{\Phi} = \Phi^-$ ; otherwise,  $\hat{\Phi} = \Phi^+$ .

If  $\mu_m \cos(\varphi_n) E_y(t, x_i, y_j) > 0$ , then  $\tilde{\Phi} = \Phi^-$ ; otherwise,  $\tilde{\Phi} = \Phi^+$ .

- The sign of  $g_5$  only depends on  $E_y(t, x, y)$ , if  $E_y(t, x_i, y_j) > 0$ , then  $\dot{\Phi} = \Phi^-$ ; otherwise,  $\dot{\Phi} = \Phi^+$ .

The schematic plot of the double gate MOSFET device is given in Figure 4.17. The shadowed region denotes the oxide-silicon region, whereas the rest is the silicon region. Since the problem is symmetric about the x-axis, we will only need to compute for  $y > 0$ . At the source and drain contacts, we implement the same boundary condition as proposed in [6] to realize neutral charges. A buffer layer of ghost points of  $i = 0$  and  $i = N_x + 1$  is used to make

$$\Phi(i = 0) = \Phi(i = 1) \frac{N_D(i = 1)}{\rho(i = 1)},$$

and

$$\Phi(i = N_x + 1) = \Phi(i = N_x) \frac{N_D(i = N_x)}{\rho(i = N_x)}.$$

At the top and bottom of the computational domain (the silicon region), we impose the classical elastic specular boundary reflection.

In the  $(w, \mu, \varphi)$ -space, no boundary condition is necessary, the reason is similar as in 1D,

- at  $w = 0$ ,  $g_3 = 0$ . At  $w = w_{\max}$ ,  $\Phi$  is machine zero;
- at  $\mu = \pm 1$ ,  $g_4 = 0$ ;
- at  $\varphi = 0, \pi$ ,  $g_5 = 0$ ,

so at the  $w, \mu, \varphi$  boundary, the numerical flux vanishes, hence no ghost point is necessary.

For the Poisson equation,  $\Psi = 0.52354$  at source,  $\Psi = 1.5235$  at drain and  $\Psi = 1.06$  at gate. For the rest of boundaries, we impose homogeneous Neumann boundary condition, i.e.,  $\frac{\partial \Psi}{\partial n} = 0$ . The relative dielectric constant in the oxide-silicon region is  $\epsilon_r = 3.9$ , in the silicon region is  $\epsilon_r = 11.7$ .

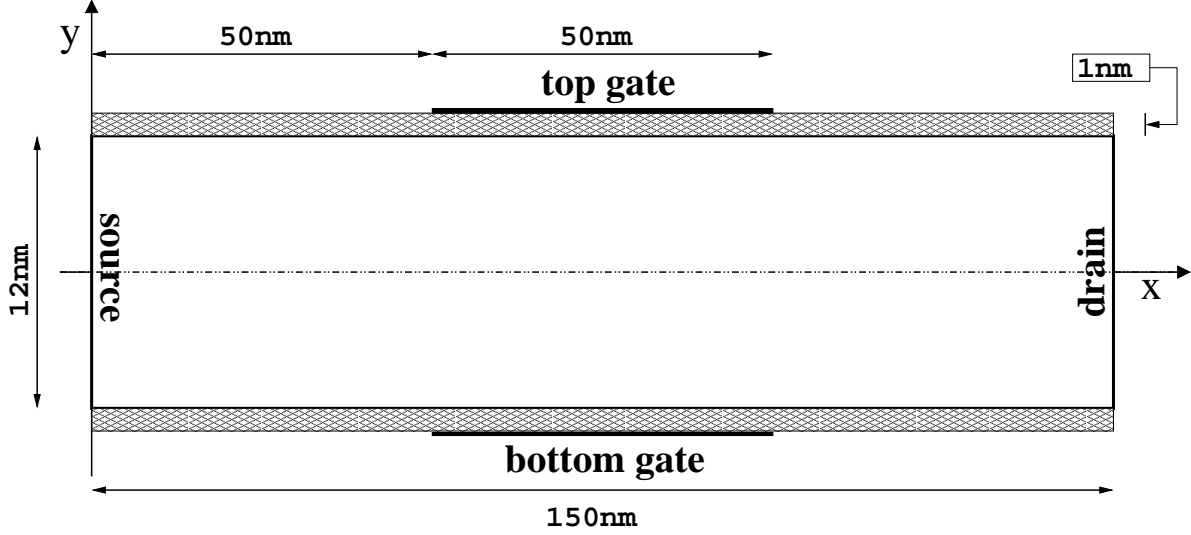


Figure 4.17: Schematic representation of a 2D double gate MOSFET device

The Poisson equation (2.11) is solved by the LDG method. It involves rewriting the equation into the following form,

$$\begin{cases} q = \frac{\partial \Psi}{\partial x}, & s = \frac{\partial \Psi}{\partial y} \\ \frac{\partial}{\partial x} (\epsilon_r q) + \frac{\partial}{\partial y} (\epsilon_r s) = R(t, x, y) \end{cases} \quad (4.22)$$

where  $R(t, x, y) = c_p [\rho(t, x, y) - \mathcal{N}_D(x, y)]$  is a known function that can be computed at each time step once  $\Phi$  is solved from (4.21), and the coefficient  $\epsilon_r$  depends on  $x, y$ . The Poisson system is only on the  $(x, y)$  domain. Hence, we use the grid  $I_{ij} = [x_{i-\frac{1}{2}}, x_{i+\frac{1}{2}}] \times [y_{j-\frac{1}{2}}, y_{j+\frac{1}{2}}]$ , with  $i = 1, \dots, N_x, j = 1, \dots, N_y + M_y$ , that includes the oxide-silicon region and is consistent with the five-dimensional rectangular grid for the Boltzmann equation in the silicon region. The approximation space is defined as

$$W_h^\ell = \{v : v|_{I_{ij}} \in P^\ell(I_{ij})\}. \quad (4.23)$$

Here  $P^\ell(I_{ij})$  denotes the set of all polynomials of degree at most  $\ell$  on  $I_{ij}$ . The LDG scheme



for (4.22) is: to find  $q_h, s_h, \Psi_h \in V_h^\ell$ , such that

$$\begin{aligned}
& \int_{I_{i,j}} q_h v_h dx dy + \int_{I_{i,j}} \Psi_h (v_h)_x dx dy - \int_{y_{j-\frac{1}{2}}}^{y_{j+\frac{1}{2}}} \hat{\Psi}_h v_h^-(x_{i+\frac{1}{2}}, y) dy + \int_{y_{j-\frac{1}{2}}}^{y_{j+\frac{1}{2}}} \hat{\Psi}_h v_h^+(x_{i-\frac{1}{2}}, y) dy = 0, \\
& \int_{I_{i,j}} s_h w_h dx dy + \int_{I_{i,j}} \Psi_h (w_h)_y dx dy - \int_{x_{i-\frac{1}{2}}}^{x_{i+\frac{1}{2}}} \tilde{\Psi}_h w_h^-(x, y_{j+\frac{1}{2}}) dx + \int_{x_{i-\frac{1}{2}}}^{x_{i+\frac{1}{2}}} \tilde{\Psi}_h w_h^+(x, y_{j-\frac{1}{2}}) dx = 0, \\
& - \int_{I_{i,j}} \epsilon_r q_h (p_h)_x dx dy + \int_{y_{j-\frac{1}{2}}}^{y_{j+\frac{1}{2}}} \widehat{\epsilon}_r q_h p_h^-(x_{i+\frac{1}{2}}, y) dy - \int_{y_{j-\frac{1}{2}}}^{y_{j+\frac{1}{2}}} \widehat{\epsilon}_r q_h p_h^+(x_{i-\frac{1}{2}}, y) dy \\
& - \int_{I_{i,j}} \epsilon_r s_h (p_h)_y dx dy + \int_{x_{i-\frac{1}{2}}}^{x_{i+\frac{1}{2}}} \widetilde{\epsilon}_r s_h p_h^-(x, y_{j+\frac{1}{2}}) dx - \int_{x_{i-\frac{1}{2}}}^{x_{i+\frac{1}{2}}} \widetilde{\epsilon}_r s_h p_h^+(x, y_{j-\frac{1}{2}}) dx \\
& = \int_{I_{i,j}} R(t, x, y) p_h dx dy \tag{4.24}
\end{aligned}$$

hold true for any  $v_h, w_h, p_h \in W_h^\ell$ . In the above formulation, we choose the flux as follows, in the  $x$ -direction, we use  $\hat{\Psi}_h = \Psi_h^-$ ,  $\widehat{\epsilon}_r q_h = \epsilon_r q_h^+ - [\Psi_h]$ . In the  $y$ -direction, we use  $\tilde{\Psi}_h = \Psi_h^-$ ,  $\widetilde{\epsilon}_r s_h = \epsilon_r s_h^+ - [\Psi_h]$ . Near the drain, we are given Dirichlet boundary condition, so we need to flip the flux in  $x$ -direction: let  $\hat{\Psi}_h(x_{i+\frac{1}{2}}, y) = \Psi_h^+(x_{i+\frac{1}{2}}, y)$  and  $\widehat{\epsilon}_r q_h(x_{i+\frac{1}{2}}, y) = \epsilon_r q_h^-(x_{i+\frac{1}{2}}, y) - [\Psi_h](x_{i+\frac{1}{2}}, y)$ , if the point  $(x_{i+\frac{1}{2}}, y)$  is at the drain. For the gate, we need to flip the flux in  $y$ -direction: let  $\tilde{\Psi}_h(x, y_{j+\frac{1}{2}}) = \Psi_h^+(x, y_{j+\frac{1}{2}})$  and  $\widetilde{\epsilon}_r s_h(x, y_{j+\frac{1}{2}}) = \epsilon_r s_h^-(x, y_{j+\frac{1}{2}}) - [\Psi_h](x, y_{j+\frac{1}{2}})$ , if the point  $(x, y_{j+\frac{1}{2}})$  is at the gate. For the bottom, we need to use the Neumann condition, and flip the flux in  $y$ -direction, i.e.,  $\tilde{\Psi}_h = \Psi_h^+$ ,  $\widetilde{\epsilon}_r s_h = \epsilon_r s_h^-$ . This scheme described above will enforce the continuity of  $\Psi$  and  $\epsilon_r \frac{\partial \Psi}{\partial n}$  across the interface of silicon and oxide-silicon interface. The solution of (4.24) gives us approximations to both the potential  $\Psi_h$  and the electric field  $(E_x)_h = -c_v q_h$ ,  $(E_y)_h = -c_v s_h$ .

To summarize, start with an initial condition for  $\Phi_h$ , the DG-LDG algorithm for the 2D double gate MOSFET advances from  $t^n$  to  $t^{n+1}$  in the following steps:

**Step 1** Compute  $\rho_h(t, x, y) = \int_0^{+\infty} dw \int_{-1}^1 d\mu \int_0^\pi d\varphi \Phi_h(t, x, y, w, \mu, \varphi)$ .

**Step 2** Use  $\rho_h(t, x, y)$  to solve from (4.24) the electric field  $(E_x)_h$  and  $(E_y)_h$ , and compute  $g_i, i = 1, \dots, 5$ .

**Step 3** Solve (4.21) and get a method of line ODE for  $\Phi_h$ .

**Step 4** Evolve this ODE by proper time stepping from  $t^n$  to  $t^{n+1}$ , if partial time step is necessary, then repeat Step 1 to 3 as needed.

All numerical results are obtained with a piecewise linear approximation space and first order Euler time stepping. Apparently the collision term makes the Euler forward time stepping stable. We use a  $24 \times 14$  grid in space, 120 points in  $w$ , 8 points in  $\mu$  and 6 points in  $\varphi$ . In Figures 4.18 and 4.19, we show the results of the macroscopic quantities. We also show the *pdf* at six different locations in the device in Figure 4.20. These *pdf*'s have been computed by averaging the values of  $\Phi_h$  over  $\varphi$ . In Figure 4.21, we present the cartesian plot for *pdf* at  $(x, y) = (0.125, 0.12)$ , where a very non-equilibrium *pdf* is observed.

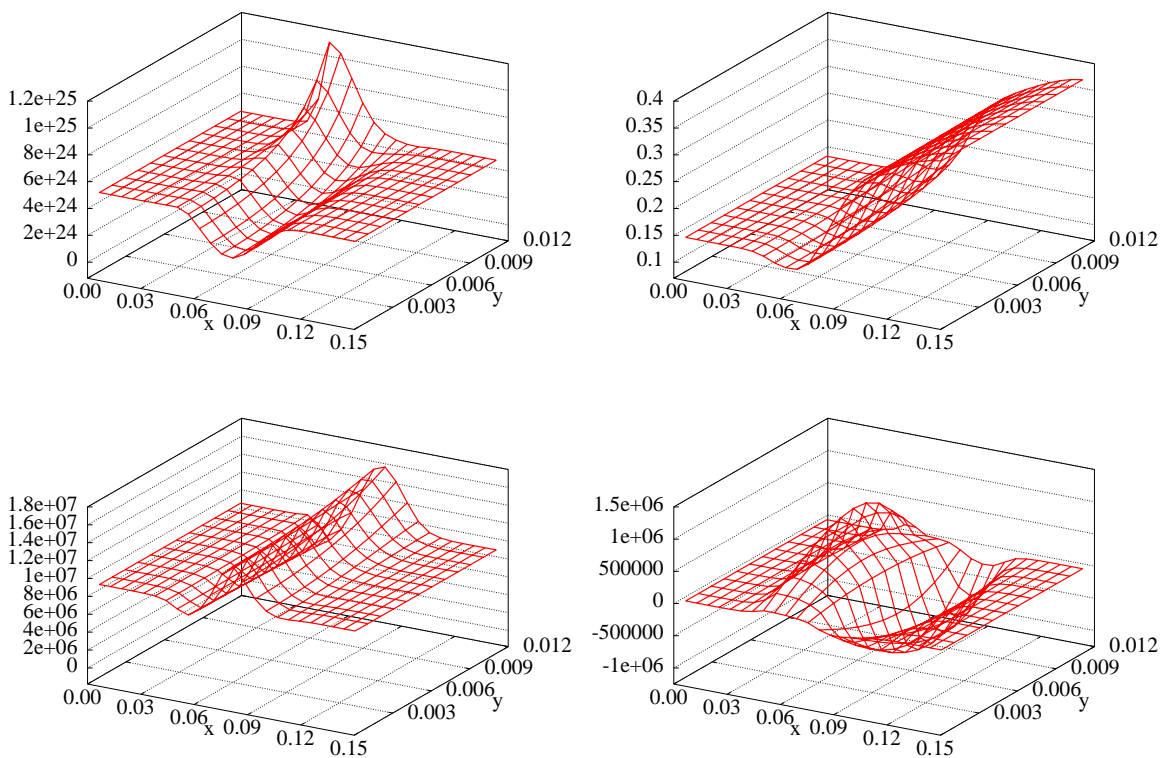


Figure 4.18: Macroscopic quantities of double gate MOSFET device at  $t = 0.5$ . Top left: density in  $cm^{-3}$ ; top right: energy in  $eV$ ; bottom left: x-component of velocity in  $cm/s$ ; bottom right: y-component of velocity in  $cm/s$ . Solution reached steady state.

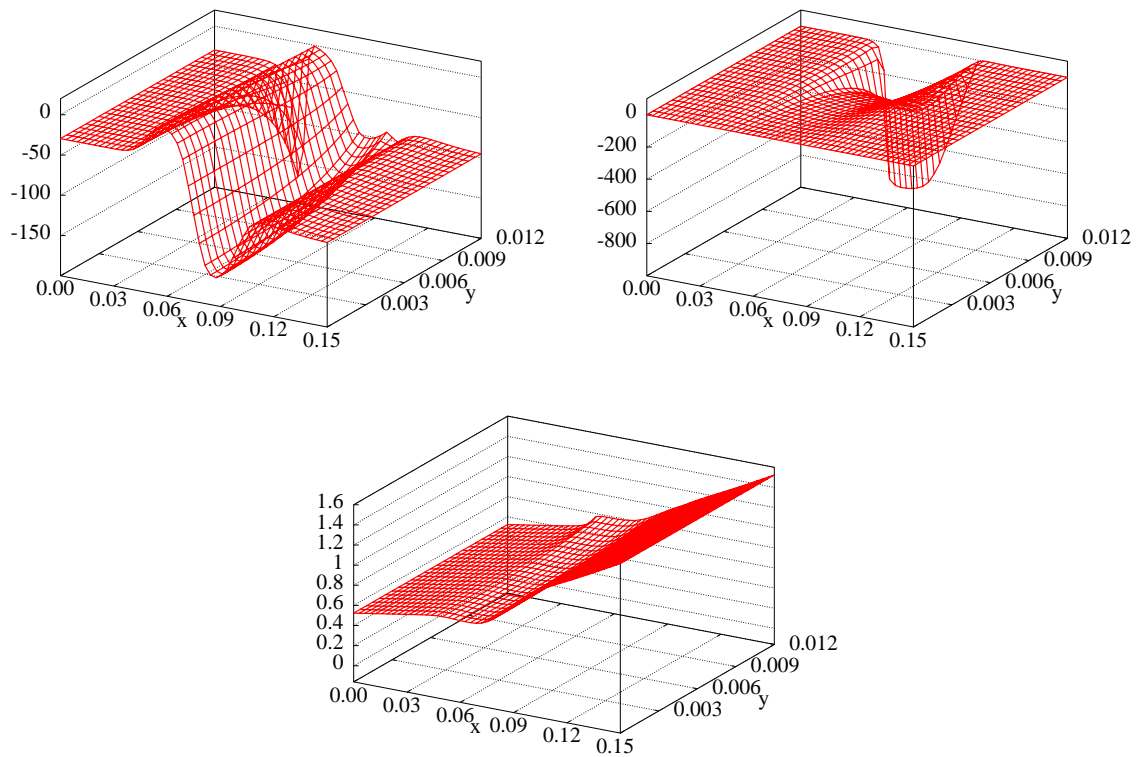


Figure 4.19: Macroscopic quantities of double gate MOSFET device at  $t = 0.5$ . Top left: x-component of electric field in  $kV/cm$ ; top right: y-component of electric field in  $kV/cm$ ; bottom: electric potential in  $V$ . Solution has reached steady state.

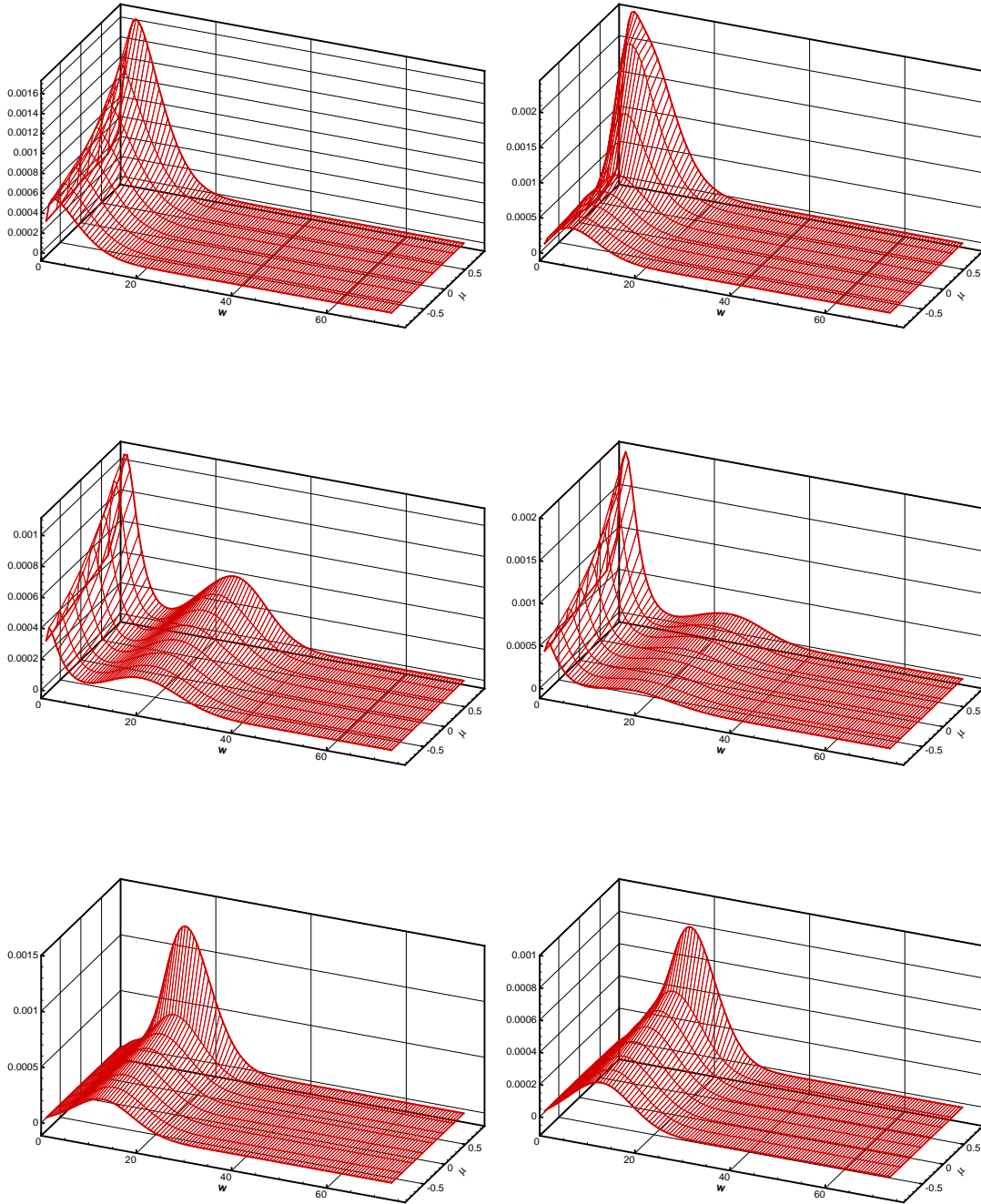


Figure 4.20: PDF of double gate MOSFET device at  $t = 0.5$ . Top left: at  $(0.025, 0.12)$ ; top right: at  $(0.075, 0.12)$ ; middle left: at  $(0.125, 0.12)$ ; middle right: at  $(0.1375, 0.06)$ ; bottom left: at  $(0.09375, 0.10)$ ; bottom right: at  $(0.09375, 0)$ . Solution reached steady state.

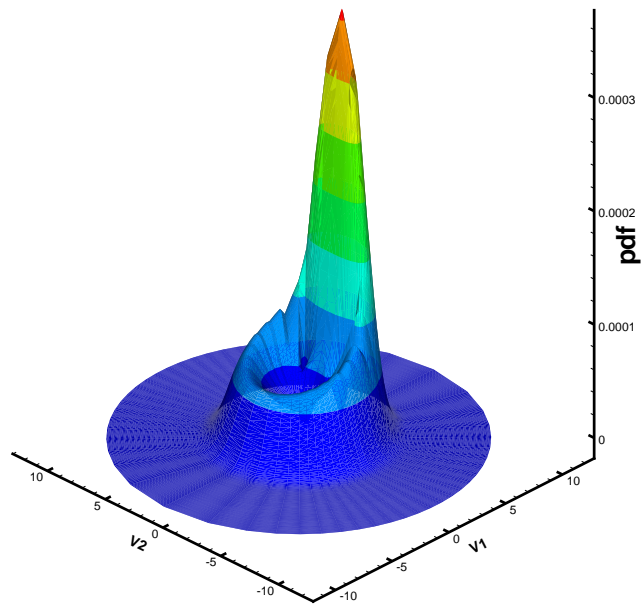


Figure 4.21: PDF for 2D double gate MOSFET at  $t = 0.5$ ,  $(x, y) = (0.9375, 0.10)$ .

## 5 Conclusions and final remarks

We have developed a DG scheme for BTEs of type (1.1), which takes into account optical-phonon interactions that become dominant under strong energetic conditions. We used the coordinate transformation proposed in [26, 4] and changed the collision into an integral-difference operator by using energy band as one of the variables. The Poisson equation is treated by LDG on a mesh that is consistent with the mesh of the DG-BTE scheme. The results are compared to those obtained from a high order WENO scheme simulation. By a local refinement in mesh, we were able to capture the subtle kinetic effects including very non-equilibrium distributions without a great increase of memory allocation and CPU time. The advantage of the DG scheme lies in its potential for implementation on unstructured meshes and for full *hp*-adaptivity. The simple communication pattern of the DG method also makes it a good candidate for the domain decomposition method for the coupled kinetic and macroscopic models.

## References

- [1] D. Arnold, F. Brezzi, B. Cockburn and L. Marini, *Unified analysis of discontinuous Galerkin methods for elliptic problems*, SIAM Journal on Numerical Analysis, 39 (2002), pp. 1749-1779.
- [2] M.J. Caceres, J.A. Carrillo, I.M. Gamba, A. Majorana and C.-W. Shu, *Deterministic kinetic solvers for charged particle transport in semiconductor devices*, in Transport Phenomena and Kinetic Theory Applications to Gases, Semiconductors, Photons, and Biological Systems. C. Cercignani and E. Gabetta (Eds.), Birkhäuser (2006), pp. 151-171.
- [3] J.A. Carrillo, I.M. Gamba, A. Majorana and C.-W. Shu, *A WENO-solver for 1D non-stationary Boltzmann-Poisson system for semiconductor devices*, Journal of Computational Electronics, 1 (2002), pp. 365-375.

- [4] J.A. Carrillo, I.M. Gamba, A. Majorana and C.-W. Shu, *A direct solver for 2D non-stationary Boltzmann-Poisson systems for semiconductor devices: a MESFET simulation by WENO-Boltzmann schemes*, Journal of Computational Electronics, 2 (2003), pp. 375-380.
- [5] J.A. Carrillo, I.M. Gamba, A. Majorana and C.-W. Shu, *A WENO-solver for the transients of Boltzmann-Poisson system for semiconductor devices. Performance and comparisons with Monte Carlo methods*, Journal of Computational Physics, 184 (2003), pp. 498-525.
- [6] J.A. Carrillo, I.M. Gamba, A. Majorana and C.-W. Shu, *2D semiconductor device simulations by WENO-Boltzmann schemes: efficiency, boundary conditions and comparison to Monte Carlo methods*, Journal of Computational Physics, 214 (2006), pp. 55-80.
- [7] Z. Chen, B. Cockburn, C. Gardner and J. Jerome, *Quantum hydrodynamic simulation of hysteresis in the resonant tunneling diode*, Journal of Computational Physics, 274 (1995), pp. 274-280.
- [8] Z. Chen, B. Cockburn, J. W. Jerome and C.-W. Shu, *Mixed-RKDG finite element methods for the 2-d hydrodynamic model for semiconductor device simulation*, VLSI Design, 3 (1995), pp. 145-158.
- [9] Y. Cheng, I. Gamba, A. Majorana and C.-W. Shu, *Discontinuous Galerkin solver for Boltzmann-Poisson transients*, Journal of Computational Electronics, 7 (2008), pp. 119-123.
- [10] Y. Cheng, I.M. Gamba, A. Majorana and C.-W. Shu, *Discontinuous Galerkin Solver for the Semiconductor Boltzmann Equation*, SISPAD 07, T. Grasser and S. Selberherr, editors, Springer (2007) pp. 257-260.

- [11] B. Cockburn, S. Hou and C.-W. Shu, *The Runge-Kutta local projection discontinuous Galerkin finite element method for conservation laws IV: the multidimensional case*, Mathematics of Computation, 54 (1990), pp. 545-581.
- [12] B. Cockburn, S.-Y. Lin and C.-W. Shu, *TVB Runge-Kutta local projection discontinuous Galerkin finite element method for conservation laws III: one dimensional systems*, Journal of Computational Physics, 84 (1989), pp. 90-113.
- [13] B. Cockburn and C.-W. Shu, *TVB Runge-Kutta local projection discontinuous Galerkin finite element method for conservation laws II: general framework*, Mathematics of Computation, 52 (1989), pp. 411-435.
- [14] B. Cockburn and C.-W. Shu, *The Runge-Kutta local projection P1-discontinuous Galerkin finite element method for scalar conservation laws*, Mathematical Modelling and Numerical Analysis, 25 (1991), pp. 337-361.
- [15] B. Cockburn and C.-W. Shu, *The Runge-Kutta discontinuous Galerkin method for conservation laws V: multidimensional systems*, Journal of Computational Physics, 141 (1998), pp. 199-224.
- [16] B. Cockburn and C.-W. Shu, *The local discontinuous Galerkin method for time-dependent convection-diffusion systems*, SIAM Journal on Numerical Analysis, 35 (1998), pp. 2440-2463.
- [17] B. Cockburn and C.-W. Shu, *Runge-Kutta discontinuous Galerkin methods for convection-dominated problems*, Journal of Scientific Computing, 16 (2001), pp. 173-261.
- [18] E. Fatemi and F. Odeh, *Upwind finite difference solution of Boltzmann equation applied to electron transport in semiconductor devices*, Journal of Computational Physics, 108 (1993), pp. 209-217.
- [19] D.K. Ferry, *Semiconductors*, Maxwell MacMillian: New-York, 1991.



- [20] M. Galler and A. Majorana, *Deterministic and stochastic simulation of electron transport in semiconductors*, to appear in Bulletin of the Institute of Mathematics, Academia Sinica (New Series), 6th MAFPD (Kyoto) special issue Vol. 2 (2007), No. 2, pp. 349-365.
- [21] I.M. Gamba and J. Proft, *Stable Discontinuous Galerkin Schemes for Linear Vlasov-Boltzmann Transport Equations*, ICES Report 07-25, submitted for publication (2007).
- [22] C. Jacoboni and P. Lugli, *The Monte Carlo method for semiconductor device simulation*, Springer-Verlag: Wien-New York, 1989.
- [23] M. Lundstrom, *Fundamentals of Carrier Transport*, Cambridge University Press: Cambridge, 2000.
- [24] Y.-X. Liu and C.-W. Shu, *Local discontinuous Galerkin methods for moment models in device simulations: formulation and one dimensional results*, Journal of Computational Electronics, 3 (2004), pp. 263-267.
- [25] Y.-X. Liu and C.-W. Shu, *Local discontinuous Galerkin methods for moment models in device simulations: Performance assessment and two dimensional results*, Applied Numerical Mathematics, 57 (2007), pp. 629-645.
- [26] A. Majorana and R. Pizatella, *A finite difference scheme solving the Boltzmann Poisson system for semiconductor devices*, Journal of Computational Physics, 174 (2001), pp. 649-668.
- [27] P.A. Markowich, C. Ringhofer and C. Schmeiser, *Semiconductor Equations*, Springer-Verlag: New-York, 1990.
- [28] K. Tomizawa, *Numerical simulation of sub micron semiconductor devices*, Artech House: Boston, 1993.
- [29] J.M. Ziman, *Electrons and Phonons. The Theory of Transport Phenomena in Solids*, Oxford University Press: Oxford, 2000.

## A Appendix

In this appendix, we collect some technical details for the implementation of the 2D DG-BTE solver. The discussion for 1D solver is similar and omitted here.

### A.1 The basis of the finite dimensional function space.

In every cell  $\Omega_{ijkmn}$ , we use piecewise linear polynomials and assume

$$\begin{aligned} \Phi_h(t, x, y, w, \mu, \varphi) = & T_{ijkmn}(t) + X_{ijkmn}(t) \frac{2(x - x_i)}{\Delta x_i} + Y_{ijkmn}(t) \frac{2(y - y_j)}{\Delta y_j} \\ & + W_{ijkmn}(t) \frac{2(w - w_k)}{\Delta w_k} + M_{ijkmn}(t) \frac{2(\mu - \mu_m)}{\Delta \mu_m} + P_{ijkmn}(t) \frac{2(\varphi - \varphi_n)}{\Delta \varphi_n}. \end{aligned} \quad (\text{A.1})$$

It will be useful to note that

$$\begin{aligned} \Phi_h(t, x, y, w, \mu, \varphi) = & \sum_{k=1}^{N_w} \left[ T_{ijkmn}(t) + X_{ijkmn}(t) \frac{2(x - x_i)}{\Delta x_i} + Y_{ijkmn}(t) \frac{2(y - y_j)}{\Delta y_j} \right. \\ & \left. + W_{ijkmn}(t) \frac{2(w - w_k)}{\Delta w_k} + M_{ijkmn}(t) \frac{2(\mu - \mu_m)}{\Delta \mu_m} + P_{ijkmn}(t) \frac{2(\varphi - \varphi_n)}{\Delta \varphi_n} \right] \chi_k(w), \end{aligned}$$

for every  $(x, y, w, \mu, \varphi) \in \bigcup_{k=1}^{N_w} \Omega_{ijkmn}$ . Here,  $\chi_k(w)$  is the characteristic function in the interval  $\left[ w_{k-\frac{1}{2}}, w_{k+\frac{1}{2}} \right]$ .

### A.2 Treatment of the collision operator

The gain term of the collisional operator is

$$\begin{aligned} G(\Phi_h)(t, x, y, w) = & s(w) \left\{ c_0 \int_0^\pi d\varphi' \int_{-1}^1 d\mu' \Phi_h(t, x, y, w, \mu', \varphi') \right. \\ & \left. + \int_0^\pi d\varphi' \int_{-1}^1 d\mu' [c_+ \Phi_h(t, x, y, w + \gamma, \mu', \varphi') + c_- \Phi_h(t, x, y, w - \gamma, \mu', \varphi')] \right\}. \end{aligned} \quad (\text{A.2})$$

Now, we define

$$(\overline{v_h})_{mn}(x, y, w) := \int_{\varphi_{n-\frac{1}{2}}}^{\varphi_{n+\frac{1}{2}}} d\varphi \int_{\mu_{m-\frac{1}{2}}}^{\mu_{m+\frac{1}{2}}} d\mu v_h(x, y, w, \mu, \varphi),$$

and, for  $\sigma = -\gamma, 0, \gamma$ , we have

$$\begin{aligned}
& \int_{\Omega_{ijkmn}} v_h(x, y, w, \mu, \varphi) \left[ s(w) \int_0^\pi d\varphi' \int_{-1}^1 d\mu' \Phi(t, x, y, w + \sigma, \mu', \varphi') \right] dx dy dw d\mu d\varphi \\
&= \int_0^\pi d\varphi' \int_{-1}^1 d\mu' \int_{x_{i-\frac{1}{2}}}^{x_{i+\frac{1}{2}}} dx \int_{y_{j-\frac{1}{2}}}^{y_{j+\frac{1}{2}}} dy \int_{w_{k-\frac{1}{2}}}^{w_{k+\frac{1}{2}}} dw s(w) \Phi(t, x, y, w + \sigma, \mu', \varphi') (\overline{v_h})_{mn}(x, y, w) \\
&= \sum_{m'=1}^{N_\mu} \sum_{n'=1}^{N_\varphi} \int_{\Omega_{ijkm'n'}} s(w) \Phi_h(t, x, y, w + \sigma, \mu', \varphi') (\overline{v_h})_{mn}(x, y, w) dx dy dw d\mu' d\varphi'.
\end{aligned}$$

Now we discuss the following integral for different test function  $v_h$ ,

$$I = \int_{\Omega_{ijkmn}} v_h(x, y, w, \mu, \varphi) \left[ s(w) \int_0^\pi d\varphi' \int_{-1}^1 d\mu' \Phi_h(t, x, y, w + \sigma, \mu', \varphi') \right] dx dy dw d\mu d\varphi.$$

- For  $v_h(x, y, w, \mu, \varphi) = 1$ ,

$$\begin{aligned}
I &= \sum_{m'=1}^{N_\mu} \sum_{n'=1}^{N_\varphi} \sum_{k'=1}^{N_w} \Delta\mu_{m'} \Delta\varphi_{n'} \left[ T_{ijk'm'n'}(t) \int_{w_{k-\frac{1}{2}}}^{w_{k+\frac{1}{2}}} s(w) \chi_{k'}(w + \sigma) dw \right. \\
&\quad \left. + W_{ijk'm'n'}(t) \int_{w_{k-\frac{1}{2}}}^{w_{k+\frac{1}{2}}} s(w) \frac{2(w + \sigma - w_{k'})}{\Delta w_{k'}} \chi_{k'}(w + \sigma) dw \right] \Delta x_i \Delta y_j \Delta\mu_m \Delta\varphi_n.
\end{aligned}$$

- For  $v_h(x, y, w, \mu, \varphi) = \frac{2(x-x_i)}{\Delta x_i}$ ,

$$\begin{aligned}
I &= \frac{1}{3} \Delta x_i \Delta y_j \Delta\mu_m \Delta\varphi_n \sum_{m'=1}^{N_\mu} \sum_{n'=1}^{N_\varphi} \sum_{k'=1}^{N_w} \Delta\mu_{m'} \Delta\varphi_{n'} X_{ijk'm'n'}(t) \\
&\quad \times \int_{w_{k-\frac{1}{2}}}^{w_{k+\frac{1}{2}}} s(w) \chi_{k'}(w + \sigma) dw.
\end{aligned}$$

- For  $v_h(x, y, w, \mu, \varphi) = \frac{2(y-y_j)}{\Delta y_j}$ ,

$$\begin{aligned}
I &= \frac{1}{3} \Delta x_i \Delta y_j \Delta\mu_m \Delta\varphi_n \sum_{m'=1}^{N_\mu} \sum_{n'=1}^{N_\varphi} \sum_{k'=1}^{N_w} \Delta\mu_{m'} \Delta\varphi_{n'} Y_{ijk'm'n'}(t) \\
&\quad \times \int_{w_{k-\frac{1}{2}}}^{w_{k+\frac{1}{2}}} s(w) \chi_{k'}(w + \sigma) dw.
\end{aligned}$$

- For  $v_h(x, y, w, \mu, \varphi) = \frac{2(w-w_k)}{\Delta w_k}$ ,

$$I = \sum_{m'=1}^{N_\mu} \sum_{n'=1}^{N_\varphi} \sum_{k'=1}^{N_w} \Delta\mu_{m'} \Delta\varphi_{n'} \left[ T_{ijk'm'n'}(t) \int_{w_{k-\frac{1}{2}}}^{w_{k+\frac{1}{2}}} s(w) \frac{2(w-w_k)}{\Delta w_k} \chi_{k'}(w+\sigma) dw \right. \\ \left. + W_{ijk'm'n'}(t) \int_{w_{k-\frac{1}{2}}}^{w_{k+\frac{1}{2}}} s(w) \frac{4(w+\sigma-w_{k'})(w-w_k)}{\Delta w_{k'} \Delta w_k} \chi_{k'}(w+\sigma) dw \right] \Delta x_i \Delta y_j \Delta\mu_m \Delta\varphi_n.$$

- For  $v_h(x, y, w, \mu, \varphi) = \frac{2(\mu-\mu_m)}{\Delta\mu_m}$ ,  $I = 0$ .

- For  $v_h(x, y, w, \mu, \varphi) = \frac{2(\varphi-\varphi_n)}{\Delta\varphi_n}$ ,  $I = 0$ .

The lost term in the collision operator is

$$2\pi[c_0 s(w) + c_+ s(w-\gamma) + c_- s(w+\gamma)] \Phi(t, x, y, w, \mu, \varphi). \quad (\text{A.3})$$

Let

$$\nu(w) = 2\pi[c_0 s(w) + c_+ s(w-\gamma) + c_- s(w+\gamma)],$$

then we need to evaluate numerically,

$$I' = \int_{\Omega_{ijkmn}} \nu(w) \Phi_h(t, x, y, w, \mu, \varphi) v_h(x, y, w, \mu, \varphi) dx dy dw d\mu d\varphi.$$

- For  $v_h(x, y, w, \mu, \varphi) = 1$ ,

$$I' = \Delta x_i \Delta y_j \Delta\mu_m \Delta\varphi_n \\ \times \left[ T_{ijkmn}(t) \int_{w_{k-\frac{1}{2}}}^{w_{k+\frac{1}{2}}} \nu(w) dw + W_{ijkmn}(t) \int_{w_{k-\frac{1}{2}}}^{w_{k+\frac{1}{2}}} \nu(w) \frac{2(w-w_k)}{\Delta w_k} dw \right].$$

- For  $v_h(x, y, w, \mu, \varphi) = \frac{2(x-x_i)}{\Delta x_i}$ ,

$$I' = \frac{1}{3} \Delta x_i \Delta y_j \Delta\mu_m \Delta\varphi_n X_{ijkmn}(t) \int_{w_{k-\frac{1}{2}}}^{w_{k+\frac{1}{2}}} \nu(w) dw.$$

- For  $v_h(x, y, w, \mu, \varphi) = \frac{2(y-y_j)}{\Delta y_j}$ ,

$$I' = \frac{1}{3} \Delta x_i \Delta y_j \Delta \mu_m \Delta \varphi_n Y_{ijkmn}(t) \int_{w_{k-\frac{1}{2}}}^{w_{k+\frac{1}{2}}} \nu(w) dw .$$

- For  $v_h(x, y, w, \mu, \varphi) = \frac{2(w-w_k)}{\Delta w_k}$ ,

$$I' = \Delta x_i \Delta y_j \Delta \mu_m \Delta \varphi_n \left[ T_{ijkmn}(t) \int_{w_{k-\frac{1}{2}}}^{w_{k+\frac{1}{2}}} \nu(w) \frac{2(w-w_k)}{\Delta w_k} dw \right. \\ \left. + W_{ijkmn}(t) \int_{w_{k-\frac{1}{2}}}^{w_{k+\frac{1}{2}}} \nu(w) \frac{4(w-w_k)^2}{(\Delta w_k)^2} dw \right] .$$

- For  $v_h(x, y, w, \mu, \varphi) = \frac{2(\mu-\mu_m)}{\Delta \mu_m}$ ,

$$I' = \frac{1}{3} \Delta x_i \Delta y_j \Delta \mu_m \Delta \varphi_n M_{ijkmn}(t) \int_{w_{k-\frac{1}{2}}}^{w_{k+\frac{1}{2}}} \nu(w) dw .$$

- For  $v_h(x, y, w, \mu, \varphi) = \frac{2(\varphi-\varphi_n)}{\Delta \varphi_n}$ ,

$$I' = \frac{1}{3} \Delta x_i \Delta y_j \Delta \mu_m \Delta \varphi_n P_{ijkmn}(t) \int_{w_{k-\frac{1}{2}}}^{w_{k+\frac{1}{2}}} \nu(w) dw .$$

### A.3 Integrals related to the collisional operator

We need to evaluate (some numerically) the following integrals

$$\begin{aligned}
& \int_{w_{k-\frac{1}{2}}}^{w_{k+\frac{1}{2}}} s(w) \chi_{k'}(w + \sigma) dw \\
& \int_{w_{k-\frac{1}{2}}}^{w_{k+\frac{1}{2}}} s(w) \frac{2(w + \sigma - w_{k'})}{\Delta w_{k'}} \chi_{k'}(w + \sigma) dw \\
& \int_{w_{k-\frac{1}{2}}}^{w_{k+\frac{1}{2}}} s(w) \frac{2(w - w_k)}{\Delta w_k} \chi_{k'}(w + \sigma) dw \\
& \int_{w_{k-\frac{1}{2}}}^{w_{k+\frac{1}{2}}} s(w) \frac{4(w + \sigma - w_{k'})(w - w_k)}{\Delta w_{k'} \Delta w_k} \chi_{k'}(w + \sigma) dw \\
& \int_{w_{k-\frac{1}{2}}}^{w_{k+\frac{1}{2}}} \nu(w) dw \\
& \int_{w_{k-\frac{1}{2}}}^{w_{k+\frac{1}{2}}} \nu(w) \frac{2(w - w_k)}{\Delta w_k} dw \\
& \int_{w_{k-\frac{1}{2}}}^{w_{k+\frac{1}{2}}} \nu(w) \left[ \frac{2(w - w_k)}{\Delta w_k} \right]^2 dw .
\end{aligned}$$

If we evaluate these integrals by means of numerical quadrature formulas, then it is appropriate to eliminate the singularity of the function  $s(w)$  at  $w = 0$  by change of variables.

$$\begin{aligned}
\int_a^b s(w) dw &= \int_a^b \sqrt{w(1 + \alpha_K w)} (1 + 2\alpha_K w) dw \\
&= \int_{\sqrt{a}}^{\sqrt{b}} \sqrt{1 + \alpha_K r^2} (1 + 2\alpha_K r^2) 2r^2 dr, \quad (w = r^2) \\
\int_a^b s(w - \gamma) dw &= \int_{a-\gamma}^{b-\gamma} s(\hat{w}) d\hat{w} \\
&= \int_{\sqrt{a-\gamma}}^{\sqrt{b-\gamma}} \sqrt{1 + \alpha_K r^2} (1 + 2\alpha_K r^2) 2r^2 dr, \quad (w = r^2 + \gamma) \\
\int_a^b s(w + \gamma) dw &= \int_{a+\gamma}^{b+\gamma} s(\bar{w}) d\bar{w} \\
&= \int_{\sqrt{a+\gamma}}^{\sqrt{b+\gamma}} \sqrt{1 + \alpha_K r^2} (1 + 2\alpha_K r^2) 2r^2 dr. \quad (w = r^2 - \gamma)
\end{aligned}$$

## A.4 Integrals related to the free streaming operator

We recall that

$$\begin{aligned}
g_1(\cdot) &= c_x \frac{\mu \sqrt{w(1 + \alpha_K w)}}{1 + 2\alpha_K w}, \\
g_2(\cdot) &= c_x \frac{\sqrt{1 - \mu^2} \sqrt{w(1 + \alpha_K w)} \cos \varphi}{1 + 2\alpha_K w}, \\
g_3(\cdot) &= -2c_k \frac{\sqrt{w(1 + \alpha_K w)}}{1 + 2\alpha_K w} \left[ \mu E_x(t, x, y) + \sqrt{1 - \mu^2} \cos \varphi E_y(t, x, y) \right], \\
g_4(\cdot) &= -c_k \frac{\sqrt{1 - \mu^2}}{\sqrt{w(1 + \alpha_K w)}} \left[ \sqrt{1 - \mu^2} E_x(t, x, y) - \mu \cos \varphi E_y(t, x, y) \right], \\
g_5(\cdot) &= c_k \frac{\sin \varphi}{\sqrt{w(1 + \alpha_K w)} \sqrt{1 - \mu^2}} E_y(t, x, y).
\end{aligned}$$

Now, we define:

$$s_1(w) = \frac{\sqrt{w(1 + \alpha_K w)}}{1 + 2\alpha_K w}, \quad s_2(w) = \frac{1}{\sqrt{w(1 + \alpha_K w)}}.$$

We need to evaluate the integrals.

$$\begin{aligned}
\int_a^b s_1(w) dw &= \int_a^b \frac{\sqrt{w(1 + \alpha_K w)}}{1 + 2\alpha_K w} dw = \int_{\sqrt{a}}^{\sqrt{b}} \frac{\sqrt{1 + \alpha_K r^2}}{1 + 2\alpha_K r^2} 2r^2 dr, \\
\int_a^b s_2(w) dw &= \int_a^b \frac{1}{\sqrt{w(1 + \alpha_K w)}} dw = \int_{\sqrt{a}}^{\sqrt{b}} \frac{2}{\sqrt{1 + \alpha_K r^2}} dr, \\
\int_a^b s_1(w) \frac{2(w - w_k)}{\Delta w_k} dw &= \int_a^b \frac{\sqrt{w(1 + \alpha_K w)}}{1 + 2\alpha_K w} \frac{2(w - w_k)}{\Delta w_k} dw \\
&= \int_{\sqrt{a}}^{\sqrt{b}} \frac{\sqrt{1 + \alpha_K r^2}}{1 + 2\alpha_K r^2} \frac{2(r^2 - w_k)}{\Delta w_k} 2r^2 dr, \\
\int_a^b s_2(w) \frac{2(w - w_k)}{\Delta w_k} dw &= \int_a^b \frac{1}{\sqrt{w(1 + \alpha_K w)}} \frac{2(w - w_k)}{\Delta w_k} dw \\
&= \int_{\sqrt{a}}^{\sqrt{b}} \frac{2}{\sqrt{1 + \alpha_K r^2}} \frac{2(r^2 - w_k)}{\Delta w_k} dr
\end{aligned}$$

$$\begin{aligned}
\int_a^b s_1(w) \left[ \frac{2(w-w_k)}{\Delta w_k} \right]^2 dw &= \int_a^b \frac{\sqrt{w(1+\alpha_K w)}}{1+2\alpha_K w} \left[ \frac{2(w-w_k)}{\Delta w_k} \right]^2 dw \\
&= \int_{\sqrt{a}}^{\sqrt{b}} \frac{\sqrt{1+\alpha_K r^2}}{1+2\alpha_K r^2} \left[ \frac{2(r^2-w_k)}{\Delta w_k} \right]^2 2r^2 dr, \\
\int_a^b s_2(w) \left[ \frac{2(w-w_k)}{\Delta w_k} \right]^2 dw &= \int_a^b \frac{1}{\sqrt{w(1+\alpha_K w)}} \left[ \frac{2(w-w_k)}{\Delta w_k} \right]^2 dw \\
&= \int_{\sqrt{a}}^{\sqrt{b}} \frac{2}{\sqrt{1+\alpha_K r^2}} \left[ \frac{2(r^2-w_k)}{\Delta w_k} \right]^2 dr.
\end{aligned}$$

## A.5 Initial condition

Since  $measure(\Omega_{ijkmn}) = \Delta x_i \Delta y_j \Delta w_k \Delta \mu_m \Delta \varphi_n$ , we have

$$\begin{aligned}
\int_{\Omega_{ijkmn}} \Phi_h(0, x, y, w, \mu, \varphi) dx dy dw d\mu d\varphi &= measure(\Omega_{ijkmn}) T_{ijkmn}(0), \\
\int_{\Omega_{ijkmn}} \Phi_h(0, x, y, w, \mu, \varphi) \frac{2(x-x_i)}{\Delta x_i} dx dy dw d\mu d\varphi &= \frac{1}{3} measure(\Omega_{ijkmn}) X_{ijkmn}(0), \\
\int_{\Omega_{ijkmn}} \Phi_h(0, x, y, w, \mu, \varphi) \frac{2(y-y_j)}{\Delta y_j} dx dy dw d\mu d\varphi &= \frac{1}{3} measure(\Omega_{ijkmn}) Y_{ijkmn}(0), \\
\int_{\Omega_{ijkmn}} \Phi_h(0, x, y, w, \mu, \varphi) \frac{2(w-w_k)}{\Delta w_k} dx dy dw d\mu d\varphi &= \frac{1}{3} measure(\Omega_{ijkmn}) W_{ijkmn}(0), \\
\int_{\Omega_{ijkmn}} \Phi_h(0, x, y, w, \mu, \varphi) \frac{2(\mu-\mu_m)}{\Delta \mu_m} dx dy dw d\mu d\varphi &= \frac{1}{3} measure(\Omega_{ijkmn}) M_{ijkmn}(0), \\
\int_{\Omega_{ijkmn}} \Phi_h(0, x, y, w, \mu, \varphi) \frac{2(\varphi-\varphi_n)}{\Delta \varphi_n} dx dy dw d\mu d\varphi &= \frac{1}{3} measure(\Omega_{ijkmn}) P_{ijkmn}(0).
\end{aligned}$$

If, for each  $(x, y)$  and  $(\mu, \varphi)$ ,

$$\Phi_h(0, x, y, w, \mu, \varphi) = \begin{cases} F(x, y) s(w) e^{-w} & \text{for } w < w_{N_w + \frac{1}{2}} \\ 0 & \text{otherwise} \end{cases}$$

and

$$F(x, y) = F_{ij} \text{ (constant)} \quad \forall (x, y) \in \left[ x_{i-\frac{1}{2}}, x_{i+\frac{1}{2}} \right] \times \left[ y_{j-\frac{1}{2}}, y_{j+\frac{1}{2}} \right],$$



then it is reasonable to assume

$$T_{ijkmn}(0) = \frac{F_{ij}}{\Delta w_k} \int_{w_{k-\frac{1}{2}}}^{w_{k+\frac{1}{2}}} s(w) e^{-w} dw, \quad (\text{A.4})$$

$$X_{ijkmn}(0) = Y_{ijkmn}(0) = 0, \quad (\text{A.5})$$

$$W_{ijkmn}(0) = 3 \frac{F_{ij}}{\Delta w_k} \int_{w_{k-\frac{1}{2}}}^{w_{k+\frac{1}{2}}} s(w) e^{-w} \frac{2(w-w_k)}{\Delta w_k} dw, \quad (\text{A.6})$$

$$M_{ijkmn}(0) = P_{ijkmn}(0) = 0. \quad (\text{A.7})$$

Recalling the definition (2.10) of the dimensionless charge density, we have

$$\rho(0, x, y) = 2\pi F(x, y) \sum_{k=1}^{N_w} \int_{w_{k-\frac{1}{2}}}^{w_{k+\frac{1}{2}}} s(w) e^{-w} dw,$$

which gives a relationship between  $F(x, y)$  and the initial charge density  $\rho$ .

## A.6 Hydrodynamical variables

If  $(x, y) \in \left[ x_{i-\frac{1}{2}}, x_{i+\frac{1}{2}} \right] \times \left[ y_{j-\frac{1}{2}}, y_{j+\frac{1}{2}} \right]$ , then

$$\begin{aligned} \rho_h(t, x, y) = & \sum_{k=1}^{N_w} \sum_{m=1}^{N_\mu} \sum_{n=1}^{N_\varphi} \left[ T_{ijkmn}(t) + X_{ijkmn}(t) \frac{2(x-x_i)}{\Delta x_i} \right. \\ & \left. + Y_{ijkmn}(t) \frac{2(y-y_j)}{\Delta y_j} \right] \Delta w_k \Delta \mu_m \Delta \varphi_n. \end{aligned} \quad (\text{A.8})$$

We define

$$\begin{aligned} \hat{T}_{ij}(t) &= \sum_{k=1}^{N_w} \sum_{m=1}^{N_\mu} \sum_{n=1}^{N_\varphi} T_{ijkmn}(t) \Delta w_k \Delta \mu_m \Delta \varphi_n \\ \hat{X}_{ij}(t) &= \sum_{k=1}^{N_w} \sum_{m=1}^{N_\mu} \sum_{n=1}^{N_\varphi} X_{ijkmn}(t) \Delta w_k \Delta \mu_m \Delta \varphi_n \\ \hat{Y}_{ij}(t) &= \sum_{k=1}^{N_w} \sum_{m=1}^{N_\mu} \sum_{n=1}^{N_\varphi} Y_{ijkmn}(t) \Delta w_k \Delta \mu_m \Delta \varphi_n. \end{aligned}$$

Therefore, for every  $(x, y) \in \left[ x_{i-\frac{1}{2}}, x_{i+\frac{1}{2}} \right] \times \left[ y_{j-\frac{1}{2}}, y_{j+\frac{1}{2}} \right]$ ,

$$\rho_h(t, x, y) = \hat{T}_{ij}(t) + \hat{X}_{ij}(t) \frac{2(x-x_i)}{\Delta x_i} + \hat{Y}_{ij}(t) \frac{2(y-y_j)}{\Delta y_j}. \quad (\text{A.9})$$

For every  $(x, y) \in \left[ x_{i-\frac{1}{2}}, x_{i+\frac{1}{2}} \right] \times \left[ y_{j-\frac{1}{2}}, y_{j+\frac{1}{2}} \right]$ , the approximate momentum in  $x$ -direction is

$$\begin{aligned}
& \sum_{k=1}^{N_w} \sum_{m=1}^{N_\mu} \sum_{n=1}^{N_\varphi} \Delta\varphi_n [g_{1,km} T_{ijkmn}(t) + g_{1w,km} W_{ijkmn}(t) + g_{1\mu,km} M_{ijkmn}(t)] \\
& + \left[ \sum_{k=1}^{N_w} \sum_{m=1}^{N_\mu} \sum_{n=1}^{N_\varphi} \Delta\varphi_n g_{1,km} X_{ijkmn}(t) \right] \frac{2(x - x_i)}{\Delta x_i} \\
& + \left[ \sum_{k=1}^{N_w} \sum_{m=1}^{N_\mu} \sum_{n=1}^{N_\varphi} \Delta\varphi_n g_{1,km} Y_{ijkmn}(t) \right] \frac{2(y - y_j)}{\Delta y_j}, \tag{A.10}
\end{aligned}$$

and the approximate momentum in  $y$ -direction is

$$\begin{aligned}
& \sum_{k=1}^{N_w} \sum_{m=1}^{N_\mu} \sum_{n=1}^{N_\varphi} [g_{2,kmn} T_{ijkmn}(t) + g_{2w,kmn} W_{ijkmn}(t) + g_{2\mu,kmn} M_{ijkmn}(t) + g_{2\varphi,kmn} P_{ijkmn}(t)] \\
& + \left[ \sum_{k=1}^{N_w} \sum_{m=1}^{N_\mu} \sum_{n=1}^{N_\varphi} g_{2,kmn} X_{ijkmn}(t) \right] \frac{2(x - x_i)}{\Delta x_i} \\
& + \left[ \sum_{k=1}^{N_w} \sum_{m=1}^{N_\mu} \sum_{n=1}^{N_\varphi} g_{2,kmn} Y_{ijkmn}(t) \right] \frac{2(y - y_j)}{\Delta y_j}, \tag{A.11}
\end{aligned}$$

where

$$\begin{aligned}
g_{1,km} &= \int_{w_{k-\frac{1}{2}}}^{w_{k+\frac{1}{2}}} \int_{\mu_{m-\frac{1}{2}}}^{\mu_{m+\frac{1}{2}}} g_1(w, \mu) dw d\mu \\
g_{1w,km} &= \int_{w_{k-\frac{1}{2}}}^{w_{k+\frac{1}{2}}} \int_{\mu_{m-\frac{1}{2}}}^{\mu_{m+\frac{1}{2}}} g_1(w, \mu) \frac{2(w - w_k)}{\Delta w_k} dw d\mu \\
g_{1\mu,km} &= \int_{w_{k-\frac{1}{2}}}^{w_{k+\frac{1}{2}}} \int_{\mu_{m-\frac{1}{2}}}^{\mu_{m+\frac{1}{2}}} g_1(w, \mu) \frac{2(\mu - \mu_m)}{\Delta \mu_m} dw d\mu \\
g_{2,kmn} &= \int_{w_{k-\frac{1}{2}}}^{w_{k+\frac{1}{2}}} \int_{\mu_{m-\frac{1}{2}}}^{\mu_{m+\frac{1}{2}}} \int_{\varphi_{n-\frac{1}{2}}}^{\varphi_{n+\frac{1}{2}}} g_2(w, \mu, \varphi) dw d\mu d\varphi \\
g_{2w,kmn} &= \int_{w_{k-\frac{1}{2}}}^{w_{k+\frac{1}{2}}} \int_{\mu_{m-\frac{1}{2}}}^{\mu_{m+\frac{1}{2}}} \int_{\varphi_{n-\frac{1}{2}}}^{\varphi_{n+\frac{1}{2}}} g_2(w, \mu, \varphi) \frac{2(w - w_k)}{\Delta w_k} dw d\mu d\varphi \\
g_{2\mu,kmn} &= \int_{w_{k-\frac{1}{2}}}^{w_{k+\frac{1}{2}}} \int_{\mu_{m-\frac{1}{2}}}^{\mu_{m+\frac{1}{2}}} \int_{\varphi_{n-\frac{1}{2}}}^{\varphi_{n+\frac{1}{2}}} g_2(w, \mu, \varphi) \frac{2(\mu - \mu_m)}{\Delta \mu_m} dw d\mu d\varphi \\
g_{2\varphi,kmn} &= \int_{w_{k-\frac{1}{2}}}^{w_{k+\frac{1}{2}}} \int_{\mu_{m-\frac{1}{2}}}^{\mu_{m+\frac{1}{2}}} \int_{\varphi_{n-\frac{1}{2}}}^{\varphi_{n+\frac{1}{2}}} g_2(w, \mu, \varphi) \frac{2(\varphi - \varphi_n)}{\Delta \varphi_n} dw d\mu d\varphi.
\end{aligned}$$

Analogously, the energy multiplied by the charge density  $\rho_h(t, x, y)$  is

$$\begin{aligned}
& \sum_{k=1}^{N_w} \sum_{m=1}^{N_\mu} \sum_{n=1}^{N_\varphi} \Delta\varphi_n \Delta\mu_m \left[ w_k \Delta w_k T_{ijkmn}(t) + \frac{(\Delta w_k)^2}{6} W_{ijkmn}(t) \right] \\
& + \left[ \sum_{k=1}^{N_w} \sum_{m=1}^{N_\mu} \sum_{n=1}^{N_\varphi} \Delta\varphi_n \Delta\mu_m w_k \Delta w_k X_{ijkmn}(t) \right] \frac{2(x - x_i)}{\Delta x_i} \\
& + \left[ \sum_{k=1}^{N_w} \sum_{m=1}^{N_\mu} \sum_{n=1}^{N_\varphi} \Delta\varphi_n \Delta\mu_m w_k \Delta w_k Y_{ijkmn}(t) \right] \frac{2(y - y_j)}{\Delta y_j}, \tag{A.12}
\end{aligned}$$

for every  $(x, y) \in \left[ x_{i-\frac{1}{2}}, x_{i+\frac{1}{2}} \right] \times \left[ y_{j-\frac{1}{2}}, y_{j+\frac{1}{2}} \right]$ .